Structural insights into late-stage photosystem II assembly by Psb32

Stefan Bohn[#1], Yat Kei Lo[#2], Jan Lambertz[#3], Jakob Meier-Credo[4], Torben Fürtges[5], Pasqual Liauw[3], Raphael Gasper-Schönenbrücher[6], Dennis Wiens[7], Julian D. Langer[4,8], Georg Hochberg[7], Eckhard Hofmann[6], Till Rudack[*5], Marc M. Nowaczyk[*3,9,10], Jan M. Schuller[*2]

# These authors contributed equally

* Corresponding authors

Email: marc.m.nowaczyk@uni-rostock.de; till.rudack@ur.de; jan.schuller@synmikro.uni-marburg.de

1 Helmholtz Munich, Institute of Structural Biology and cryoEM Platform, Ingolstädter Landstraße 1, 85764 Neuherberg, Germany

2 CryoEM of Molecular Machines, SYNMIKRO Research Center and Department of Chemistry, Philipps University of Marburg, Marburg, Germany

3 Plant Biochemistry, Faculty of Biology and Biotechnology, Ruhr-University Bochum, Universitätsstraße 150, 44801 Bochum, Germany

4 Proteomics, Max Planck Institute of Biophysics, Frankfurt am Main, Germany

5 Structural Bioinformatic, Regensburg Center for Biochemistry, Regensburg Center for Ultrafast Nanoscopy, Faculty of Biology and Preclinical Medicine, University of Regensburg, Regensburg, Germany

6 Protein Crystallography, Faculty of Biology and Biotechnology, Ruhr-University Bochum, Bochum, Germany

7 Evolutionary Biochemistry Group, Max Planck Institute for Terrestrial Microbiology, Marburg, Germany

8 Proteomics, Max Planck Institute for Brain Research, Frankfurt am Main, Germany

9 Department of Biochemistry, Institute of Biosciences, University of Rostock, 18059 Rostock, Germany

10 Department Life, Light, Matter, University of Rostock, 18059 Rostock, Germany

Abstract

Photosystem II (PSII) assembly is a stepwise process in which intermediate complexes with auxiliary proteins are transiently formed to allow efficient *de novo* biogenesis or repair of damaged PSII. In particular, the role of extrinsic PSII subunits (PsbO, PsbU, PsbV) and auxiliary proteins such as Psb27 for the formation and photoactivation of the Mn_4O_5Ca cluster, which catalyzes the unique water splitting reaction in mature PSII, remains unclear. Using cryo-electron microscopy, we have determined the structure of two novel late-stage PSII assembly intermediates from *Thermosynechococcus vestitus* BP-1. In contrast to previous studies, the resulting monomeric PSII complexes contain both PsbJ and Psb27 and exhibit a fully mature acceptor side, while the oxygen evolving complex (OEC) is still in an immature state. The second complex additionally associates with the late-acting assembly factor Psb32 and the extrinsic subunit PsbV. While Psb32 has received little attention, its proposed role in the complex challenges the previous assumption that all extrinsic subunits associate spontaneously, as well as the notion that PsbO initiates binding and solely drives OEC formation. Our structures of the Psb27-PSII and Psb32-PSII intermediates provide novel insights, how structural changes of C-termini of the D1 and D2 core proteins regulate maturation of the OEC and how the catalytic side is prepared for binding of the Mn_4O_5Ca cluster. The Psb32-PSII complex potentially represents the final PSII assembly intermediate that precedes the incorporation and photoactivation of the Mn_4O_5Ca cluster, allowing us to explain the final steps in the PSII biogenesis and assembly pipeline in great detail, as only the two extrinsic subunits PsbO and PsbU are missing.

Introduction

Photosystem II (PSII) is a central membrane protein complex responsible for the light-driven oxidation of water in oxygenic photosynthesis[1]. In cyanobacteria, PSII exists as both a monomer and a dimer, with each monomer consisting of more than 20 subunits. The redox cofactors involved in intrinsic electron transport are mainly coordinated by the central proteins D1 (PsbA) and D2 (PsbD), which form the heterodimeric PSII core[2]. Surrounding them are the antenna proteins CP43 (PsbC) and CP47 (PsbB), which bind a large fraction of the chlorophyll *a* (Chl *a*) molecules responsible for absorbing light energy. This energy is then transferred to reaction center (RC) P680, where charge separation takes place. In addition, 13 low-molecular-weight proteins (LMWPs) bind to the complex and are located at the periphery, helping to bind cofactors and stabilize the complex[3]. Water oxidation is catalyzed by the oxygen-evolving complex (OEC), a Mn_4O_5Ca coordinated at the lumenal side of the complex[4,5]. In cyanobacteria, the extrinsic subunits PsbO, PsbU, and PsbV separate and protect the OEC from the thylakoid lumen[6].

PSII biogenesis in cyanobacteria is subject to careful orchestration controlled by a number of assembly factors that do not occur in the functional complex[7,8]. Remarkably, the number of assembly factors involved in PSII biogenesis exceeds that of the subunits[9]. After formation of the reaction center complex (RCC), a pre-module composed of CP47 and several LMWPs associates, leading to the formation of RC47. This intermediate, together with the pre-existing CP43 module, forms a transient unit called PSII-I, which includes all major intrinsic subunits as well as the assembly factors Psb27, Psb28 and Psb34[10]. The presence of Psb28 and Psb34 leads to significant structural changes on the acceptor side of PSII. In particular, the altered orientation of D1-Glu244, D1-Tyr246 and D2-Glu241 prevents the association of bicarbonate (BIC) with the non-heme iron, similar to the reaction centers in non-oxygenic photosynthetic bacteria. This likely results in a shift of the Q_A/Q_A redox potential towards a more positive value, protecting the immature complex from oxidative damage by facilitating safe charge recombination[10]. Psb27 binds to the lumenal side of the complex, where it stabilizes the E-loop of CP43 in a configuration similar to that of active PSII. This stabilization may support photoactivation of the OEC during PSII biogenesis[10–13].

To date, all structurally resolved Psb28-containing complexes do not contain the LMWP PsbJ[10,14], suggesting that PsbJ binding is the next step in PSII biogenesis after Psb28-PSII formation. It is hypothesized that PsbJ binding triggers structural reorganization leading to dissociation of Psb28 and Psb34[10,14]. Finally, the extrinsic subunits PsbO, PsbU, and PsbV bind to the lumenal PSII site and the OEC is formed in the process of photoactivation after the release of Psb27[7,15]. However, our knowledge of the exact sequence of events leading to the formation of active PSII remains limited.

Among the proteins thought to play a role in both the late steps of PSII assembly and repair is the protein TLP18.3/Psb32[16]. Psb32 abundance was found to be reduced in a PsbV deletion strain[17], indicating a functional link between these two proteins and suggesting its potential role as a late-acting assembly factor. This protein family is conserved among plants, algae, and cyanobacteria[18] . The majority of the polypeptide contains a domain of unknown function (DUF477), also known as the TPM domain[19]. *In vitro* studies have shown that *A. thaliana* Psb32 (or AtTLP18.3) has low acid phosphatase activity[19,20]. Deletion mutants of Psb32 exhibit a distinct phenotype only under light stress conditions, characterized by impaired oxygen evolution and PSII repair, together with reduced levels of dimeric PSII[16]. However, the precise role of Psb32 in the PSII life cycle remains poorly understood.

In our current investigation, we have elucidated two previously uncharacterized structures of PSII intermediates using cryo-electron microscopy (cryo-EM). In contrast to previous studies focusing on immature PSII complexes, these complexes were isolated using Twin-Strep-tagged Psb27 without deletion of additional PSII components. The resulting monomeric PSII complexes contain both PsbJ and Psb27 and exhibit a fully mature acceptor side. In addition, one of these complexes is associated with PsbV and the late-acting assembly factor Psb32. This particular complex probably represents the ultimate PSII assembly intermediate that precedes incorporation of the Mn_4O_5Ca cluster and thus photoactivation.

Results

Potential PSII intermediates with bound Psb27 were isolated by affinity chromatography using a Twin-Strep-tag (TS-tag) fused to the N-terminus of Psb27 (see Supplemental Fig. S1 and S2) from *Thermosynechococcus vestitus* BP-1 and subsequently analyzed by single-particle cryo-electron microscopy (see Supplemental Fig. S3A). Because these biogenesis intermediates are present at extremely low abundance, cryo-EM analysis required purification conditions that maximize stability and particle recovery. We therefore replaced DDM with lauryl maltose neopentyl glycol (LMNG), which forms exceptionally stable and uniform micelles that preserve native transmembrane architecture while remaining tightly associated with the protein[21]. This strong association allows extensive removal of free detergent without compromising integrity, enabling vitrification under detergent-minimized conditions that greatly increased particle yield. Using this method, we obtained two high-resolution maps, which allowed reliable modeling with excellent statistical parameters (see Supplementary Table S1 and Figs. S3B-D, S4). The first map, with a resolution of approximately 2.8 Å, termed Psb27-PSII, represents a monomeric PSII complex that includes nearly all membrane-bound subunits (including D1, D2, CP43, CP47, Cyt b_{559}, PsbH, PsbI, PsbJ, PsbK, PsbL, PsbM, PsbT, PsbX, PsbZ, Psb30) in addition to the assembly factor Psb27. Notably absent are the extrinsic proteins of mature PSII (PsbO, PsbU, PsbV) and the small single transmembrane helix subunit PsbY (Fig. 1A). The second map, at 2.9 Å resolution, designated Psb32-PSII (see Fig. 1), also represents a monomeric assembly intermediate containing all proteins as in Psb27-PSII and additionally the extrinsic subunit PsbV and the assembly factor Psb32. The presence of all assigned proteins was confirmed by mass spectrometry analysis (see Supplementary Fig. S5, Supplementary Data 1 and 2). In addition, all cofactors characteristic of mature PSII are present in both assembly intermediates, with the exception of the Mn_4O_5Ca cluster.

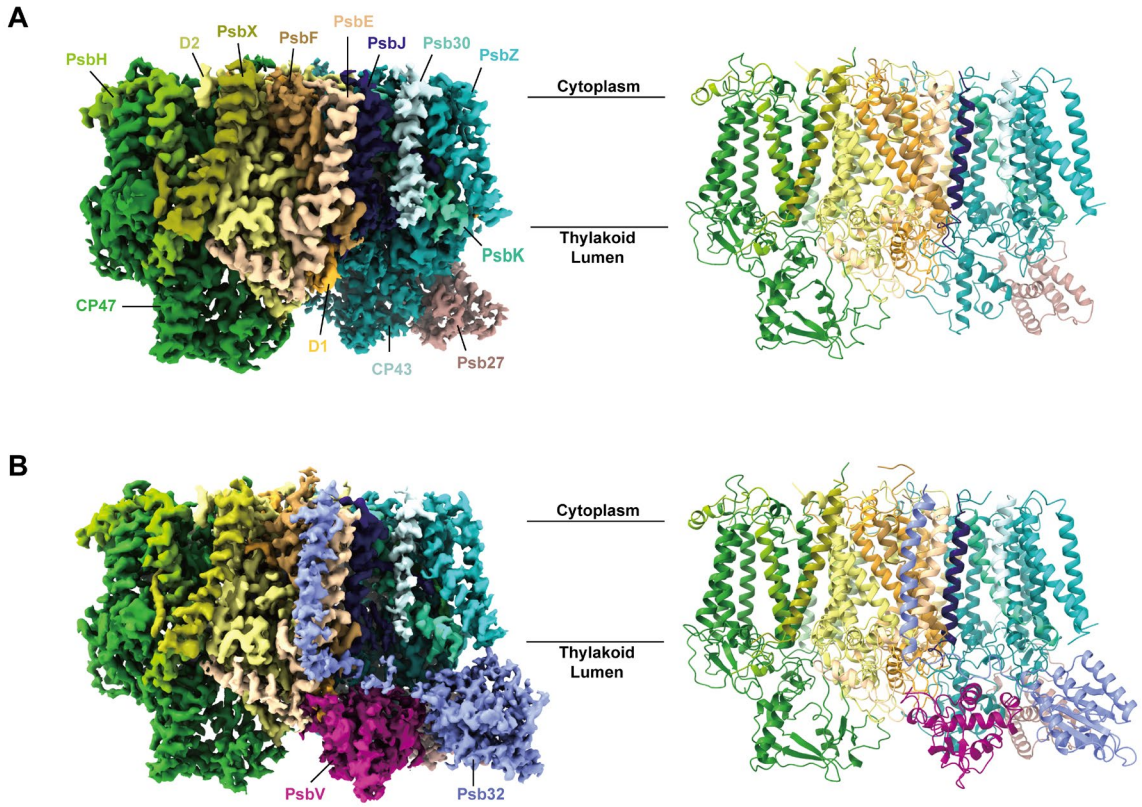

Figure 1: Structural overview of PSII assembly intermediates. Front view of the cryo-EM electron density and cartoon model of **A)** Psb27-PSII, and **B)** Psb32-PSII. Psb27-PSII is composed of the core PSII subunits: D1, D2, CP43, CP47, PsbE, PsbF, PsbH, PsbI, PsbJ, PsbK, PsbL, PsbM, PsbT, PsbX, PsbZ, Psb30, and the auxiliary protein Psb27. Psb32-PSII additionally binds Psb32 and the extrinsic subunit PsbV.

Previous structural studies of Psb27-containing PSII assembly intermediates were based on complexes that were either isolated from a *psbJ* knockout strain[10] or PsbJ was potentially lost during sample preparation[14,22,23], resulting in an empty Q_B-binding pocket. Interestingly, Psb27-PSII and Psb32-PSII of this study both contain PsbJ and Q_B (Fig. 2). This suggests that the binding of PsbJ may complete the maturation of the PSII acceptor side by contributing to the formation of the Q_B binding pocket. The absence or low abundance of Psb28-containing PSII intermediates in our TS-Psb27 preparation from wild-type background suggests that PsbJ binding triggers or promotes the release of Psb28 as well as Psb34 from PSII-I to yield Psb27-PSII[10,14].

To investigate the influence of Psb32-PSII complex formation on Psb32, we additionally resolved the structure of the soluble domain of Psb32 from *T. vestitus* fused to superfolder GFP (sfGFP) at a resolution of 2.12 Å by X-ray crystallography (see Supplementary Fig. S6, Supplementary Table S2). Our structural model (PDB-ID 8C7I) demonstrates an excellent overlap (Cα RMSD 1.74 Å, 149 atoms) with

an earlier X-ray crystal structure of *A. thaliana* Psb32 (PDB-ID: 3PVH)[19], except for the N-terminal helix 1, which shows partial unfolding in cyanobacterial Psb32 (see Supplementary Fig. S7).

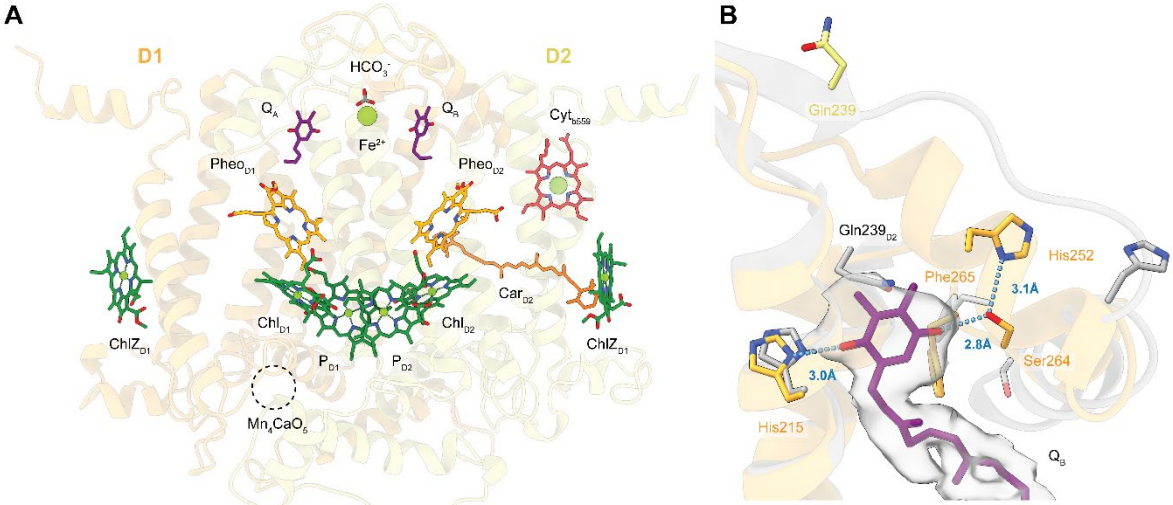

Figure 2: Cofactors of the Psb32-PSII assembly intermediate. A) Overview of cofactors assigned according to observed electron density in Psb32-PSII (PDB ID: 9I83). **B)** Zoom-in view of Psb32-PSII Q_B binding site, super-positioned with PSII-I (PDB ID: 7NHP) Psb32-PSII Q_B site adapted the mature PSII configuration, in which D1 His215, His252, and Ser264 are in position to coordinate Q_B. D1 and D2 subunits of Psb32-PSII are colored in orange and yellow, respectively. PSII-I is colored in grey. The density of Q_B is shown at 5.8 σ.

There are no significant differences between the backbone fold of the soluble domain of PSII-bound Psb32 of the cryo-EM structure and the isolated domain of the X-ray crystal structure (Cα RMSD 0.66 Å, 149 atoms). However, Psb32 is a tail-anchored protein, and by a detailed examination of our Psb32-PSII cryo-EM density we identified its C-terminal transmembrane helix (TMH, residues D198 to S228), which is approximately 40 Å away from the soluble domain (Fig. 3A). The globular domain (residues S32 to K172) and the TMH are connected via a long linker (G173 to T197). The TMH is located at the position of PsbY in active PSII (PDB ID 4PJ0)[24] near the heme of Cyt b_{559} (Fig. 3A). Psb32 and PsbY both interact with PsbE mainly due to hydrophobic interactions (Fig. S8). The proximity of the C-terminal helix of Psb32 to Cyt b_{559} is of particular interest as Cyt b_{559} is involved in alternative electron pathways within PSII that contribute to photoprotection[25], consistent with the proposed role of Psb32 in protection against ROS[18]. Although the overall induced changes to the coordination of Cyt b_{559} are negligible within the limits of resolution, Psb32 could possibly affect its redox properties.

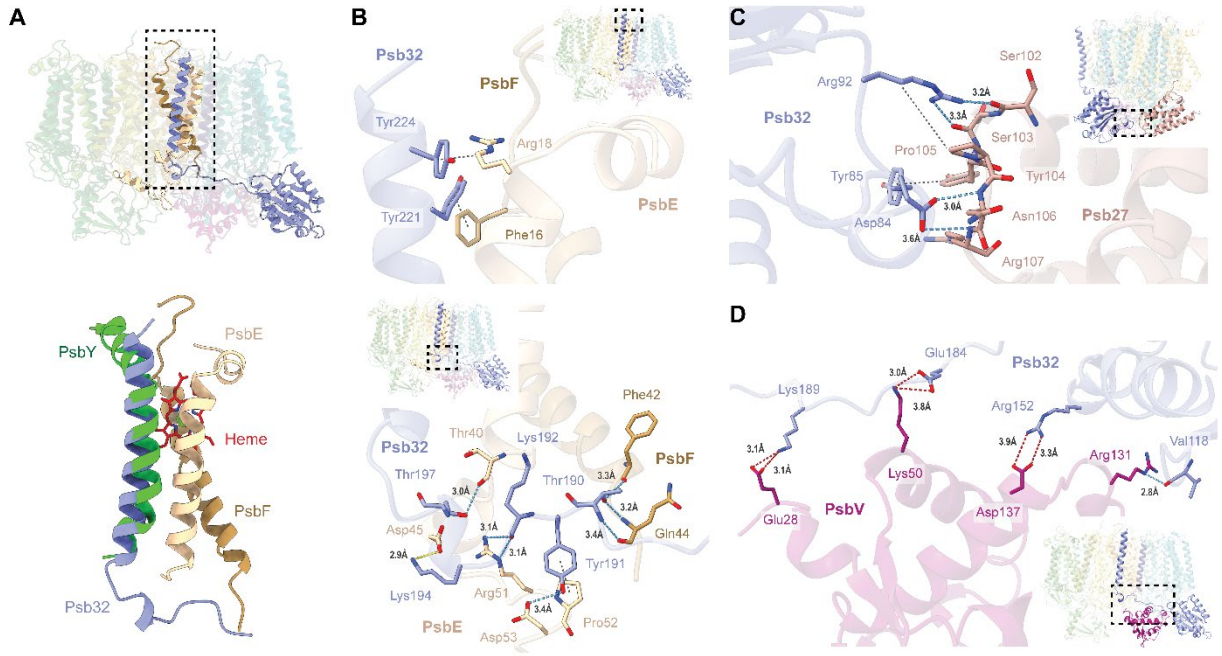

Figure 3: Psb32 interacts with PSII core subunits and assembly factors. A) Enlarged view of Psb32-PSII Cyt b_{559} (boxed region), super-positioned with PsbY from the mature PSII (PDB ID: 4PJ0). In mature PSII, the heme group is enclosed by PsbE, PsbF, and PsbY, while in Psb32-PSII, the C-terminal transmembrane helix of Psb32 binds at the position of PsbY which can influence the potential of Cyt b_{559}. **B-D)** Zoom-in view of specific interactions between Psb32, Psb27, PsbE, or PsbF with highlighted hydrogen bonds (blue dashed lines), salt-bridges (yellow dashed lines) and hydrophobic interaction pairs (grey dashed lines). Position of the interaction interface is illustrated in the inserts.

Only the Psb32 TMH interacts with the PSII core complex through PsbE and PsbF (Fig. 3B, C, Fig. S8, Table S3). The Psb32 soluble domain interacts with the assembly factor Psb27 and the extrinsic subunit PsbV (Fig. 3D, E). In the current structure, PsbV is located almost at its mature position near the lumenal loop regions of CP43 (residues 386-397 and 412-417) and D1 proteins (residues 305-315) (detailed in Supporting Table S3). The primary interaction motive between Psb32 and Psb27 is localized within the Psb32 loop from residues Leu80 to Pro89 and the Psb27 loop from residues Ser102 to Glu11. Precisely, the loop residues Arg82 and Asp84 of Psb32 as well as Ser102, Ser103, and Asn106, Arg107 of Psb27 form hydrogen bonds (Fig. 3D). Additionally, Psb32 Tyr85 and Psb27 Tyr104 form a specific van der Waals contact. The interface between Psb32 and PsbV is stabilized by salt bridges (Psb32 Arg152 with PsbV Asp137; Psb32 Glu184 with PsbV Lys50) and a hydrogen bond (Psb32 Val118 with PsbV Arg131) primarily involving the PsbV loop from residues Lys103 to Glu135 (Fig. 3E). Overall, these interfaces are relatively small, suggesting that the interaction between PsbV and Psb32 is transient and designed for easy detachment of Psb32 from the complex, a characteristic typical of biogenesis factors[26].

180 Interestingly, while plastids encode only Psb32 (TLP18.3), cyanobacteria also encode a Psb32-like pro-
181 tein that differs from other bacterial Psb32-like proteins by possessing one or more long insertions near
182 the C-terminus, which are not well conserved (Fig. S9). The precise function of this homolog and
183 whether it could serve as an isoform capable of replacing Psb32 in the assembly process remains unclear.
184 Structure predictions for the entire Psb32-PSII assembly intermediate with a hypothetical model replac-
185 ing Psb32 with the Psb32-like protein, suggest that the putative transmembrane helix (TMH) of Psb32-
186 like protein does not bind stably to PSII in contrast to a stable bound Psb32 THM (Fig. S10). The com-
187 parison of structure predictions of the isolated Psb32-like protein with Psb32 indicates a clear difference
188 in prediction confidence and structure of the C-terminal tail (Fig. S11). Phylogenetic analysis shows that
189 Psb32-homologs are found in a wide range of non-photosynthetic bacteria and that these homologs form
190 an outgroup to the cyanobacterial proteins. Like the cyanobacterial variant, they carry a glycine-rich C-
191 terminal extension, which is not present in Psb32 (Fig. S9). The loss of this extension thus may have
192 played a role in the transition to chaperone functionality. Both Psb32-like proteins and Psb32 do not
193 appear to be present in the basal branching cyanobacterial order *Gloeobacterales*. One possible expla-
194 nation for this is that a Psb32-like precursor was transferred to an ancient cyanobacterium after *Gloeo-*
195 *bacterales* branched off from other cynaobacteria and subsequently duplicated to give the Psb32 and
196 Psb32-like clades in cyanobacteria. Alternatively, a Psb32-like protein existed in the last common an-
197 cestor of all cyanobacteria but was lost along the lineage to *Gloebacterales*. This protein would have
198 then undergone duplication in the last common ancestor of all cyanobacteria excluding *Gloeobacterales*.
199 These data show that Psb32 ultimately derives from a protein that originated in non-photosynthetic bac-
200 teria, which probably could not interact with PSII. Psb32 therefore most likely represents a case of
201 neofunctionalization after gene duplication and a rare example in which the evolutionary origins of a
202 novel assembly factor can still be reconstructed.

203 To further investigate the conformational changes required for OEC maturation, we compared the struc-
204 tures of PSII-I, Psb27-PSII, Psb32-PSII, and mature PSII in detail. Our analyses show no significant
205 differences in the global fold between our biogenesis intermediates and the mature structure (Fig. S12A-
206 D) but detailed changes in the OEC-coordinating residues. The most notable difference lies in the con-
207 formation of the D1 (His332-Ala344) and D2 C-terminal tails (Asn350-Leu352).

208 In the mature PSII structure, the D2 C-terminus points toward the D1 C-terminus (Fig. 4B), whereas in
209 the immature Psb32-PSII structure, it is flipped away, obstructing PsbO binding. This observation aligns
210 with previous studies that suggest reduced PsbO binding affinity in the presence of Psb27 and propose
211 that simultaneous binding of these factors is transient[10,14,23,27,28]. In mature PSII, the D2 C-terminus in-
212 teracts with both PsbU and PsbO (Fig 4C, D, Table S4). The spatial position of D2 Arg348 whose side
213 chain forms a hydrogen bond with the PsbU Lys104 C-terminus of the mature conformation is main-
214 tained also in the immature conformation. However, a backbone-backbone interaction between D2
215 Ala351 and PsbU Gly101 is only possible in the mature conformation. The observed D2 terminus flip
216 suggests that PsbU may stabilize the D2 C-terminus in a position that, in turn, could stabilize the D1 C-
217 terminus. Whether the conformational change of the D2 C-terminus drives or results from the binding
218 of the extrinsic subunits PsbO and PsbU is the focus of current ongoing studies.

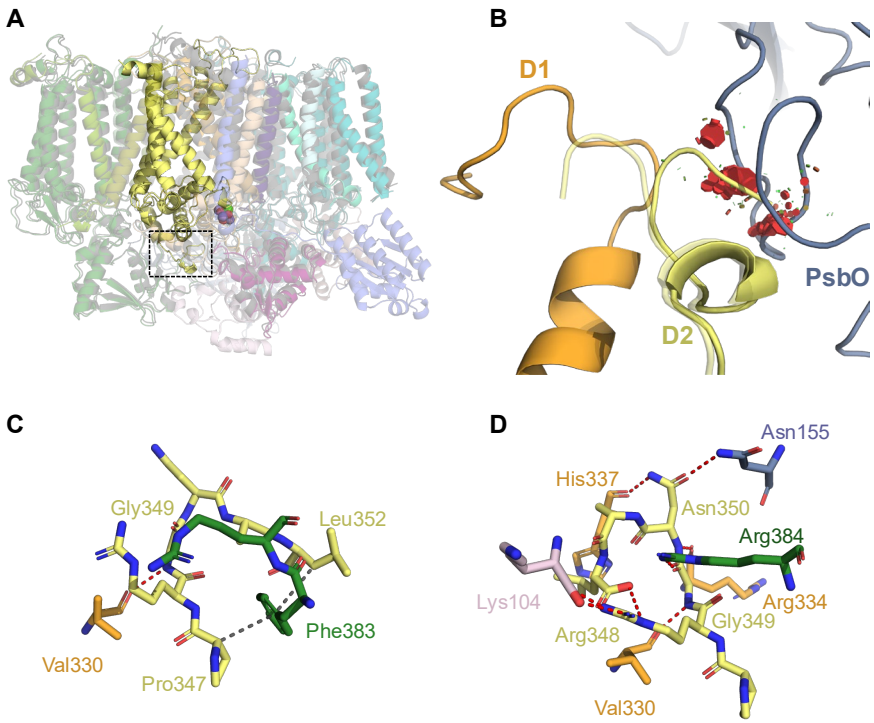

219

220 **Figure 4: Conformational change of D2 C-terminal tail. A)** Superposition of the mature PSII (grey)
221 and Psb32-PSII complex (subunit coloring as in Fig. 1). **B)** Close-up of the D2 terminal region (as
222 marked in A) reveals a steric clash between the D2 C-terminal tail residues in Psb32-PSII and PsbO
223 in the mature PSII. In contrast the D2 C-terminus of the mature PSII (transparent) is position towards
224 the D1 C-Terminus. **C)** D2 C-terminus stabilizing interactions in Psb32-PSII. The D2 C-terminus is
225 mainly stabilized by CP47 (green). **D)** D2 C-terminus stabilizing interactions in mature PSII. The ter-
226 minus interacts with D1 (orange), PsbU (pink), and PsbO (blue).

227 In all our structures at least the end of the C-terminal tail of D1, which contains the residues D1-Asp342
228 and D1-Ala344 involved in coordination of the Mn_4O_5Ca cluster, is highly flexible, as observed in other
229 PSII biogenesis intermediates earlier. Consistent with this, no clear electron density corresponding to
230 the Mn_4O_5Ca cluster is observed, though some weak density at low thresholds indicates minor sub-
231 stoichiometric binding or the presence of mixed populations that cannot be separated by further classi-
232 fication (Fig. S13D-F). This concludes that the observed Psb32-PSII intermediate is in an immature state,
233 in which the residues involved in binding of the Mn_4O_5Ca cluster are already in their final position as in
234 mature PSII – except for D1-Asp342 and D1-Ala344 - but the Mn_4O_5Ca cluster itself is mainly not
235 present or not yet stably bound. A small subpopulation of particles may contain a fully assembled
236 Mn_4O_5Ca cluster, but slightly displaced from its mature position, as indicated by a weak density in this
237 area. The observed displacement could either mean that the cluster is stalled in a non-functional state,
238 or it could also be an artifact of radiation damage. All in all, binding of PsbO (and PsbU) appears nec-
239 essary to finally position D1 Asp342 and Ala344 in a catalytic active position, enabling the formation,
240 photoactivation and stable binding of the Mn_4O_5Ca cluster to achieve final maturation of the OEC-co-
241 ordinating residues.

242 We identified D1 His332 and D1 Glu333 as key residues reflecting the progression of the OEC towards
243 its mature state. In the PSII-I structure, His332 adopts an immature conformation, oriented away from
244 the Mn_4O_5Ca cluster binding site and coordinating a chloride ion via its protonated Nδ atom (Fig. 5A).
245 In Psb27-PSII, His332 exhibits a mixture of both the immature, chloride-coordinating conformation and
246 the mature conformation, in which D1 His332 interacts with D1 Glu329 (Fig. 5B). In contrast, in Psb32-
247 PSII, D1 His332 shifts to its mature orientation, enabling coordination of the Mn_4O_5Ca cluster. In both
248 the mature PSII and Psb32-PSII structures, the mature conformation of D1 His332 is stabilized by a
249 hydrogen bond between the backbone of D1 Glu329 and the protonated D1 His332 Nδ atom (Fig 5C).
250 Similarly, D1 Glu333 undergoes a pronounced conformational change between Psb27-PSII and Psb32-
251 PSII. In Psb27-PSII, the backbone position of D1 Glu333 suggests its side chain is oriented away from
252 the Mn_4O_5Ca cluster binding pocket similar as in PSII-I (Fig. 5D). However, in Psb32-PSII, the density
253 for D1 Glu333 reveals a side chain shift enabling to point towards the Mn_4O_5Ca cluster, adopting a
254 mature conformation (Fig. 5E). All other resolved residues that coordinate the Mn_4O_5Ca cluster in the

mature complex, namely D1 D170 as well as CP43 E342 and R345, have already adopted their mature conformation, prepared for OEC incorporation (Fig. 5F). Our structural analysis indicates that the conformational transitions of His332 and Glu333 act as a critical molecular switch, governing the assembly of the OEC. Notably, Psb32 and PsbV appear to initiate these transitions, underscoring their role during the final steps of PSII biogenesis.

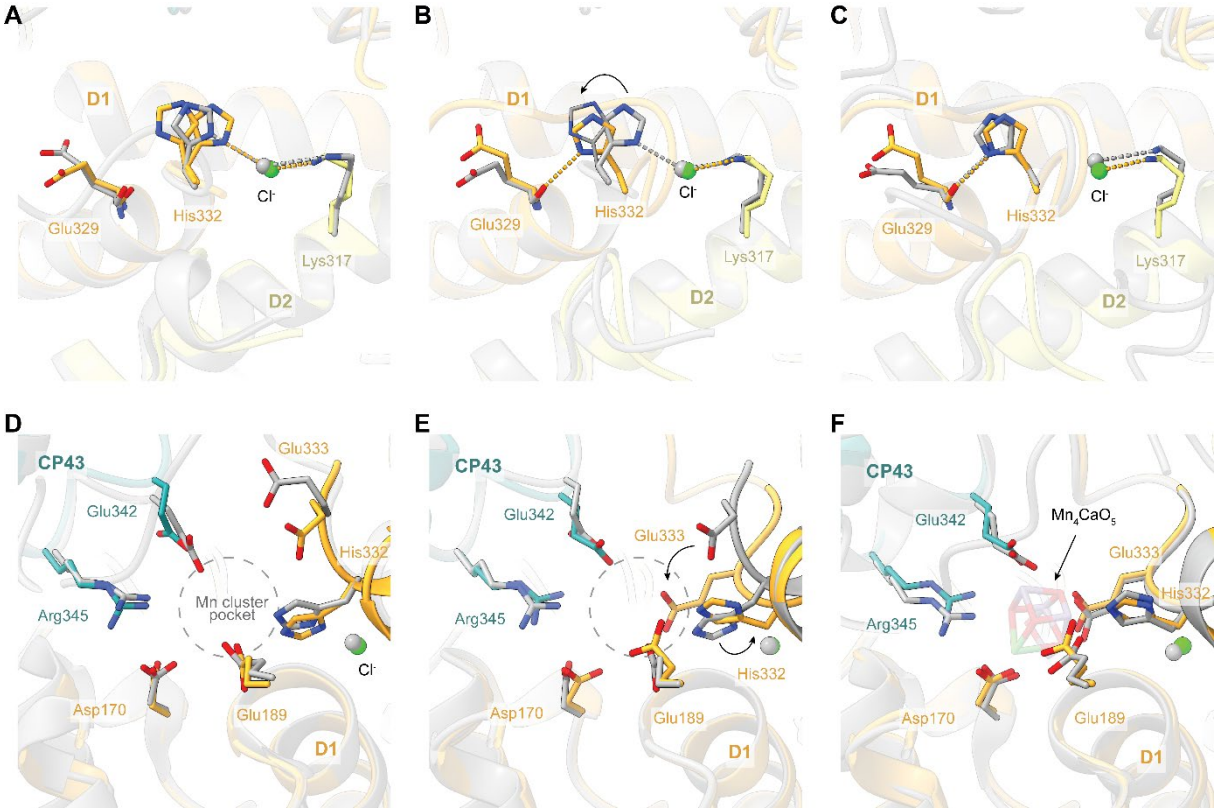

Figure 5: Maturation of the Mn_4O_5Ca **pocket. A)** Superposition of PSII-I (grey, PDB-ID: 7NHP) and Psb27-PSII (PDB-ID 9I82), **B)** Psb27-PSII (grey) and Psb32-PSII (PDB-ID 9I83), and **C)** Psb32-PSII and mature PSII (grey, PDB-ID: 4PJ0). In **A-C** the conformational changes of His332 of D1 are highlighted. **D)** Superposition of OEC between PSII-I (grey) and Psb27-PSII, **E)** Psb27-PSII (grey) and Psb32-PSII, and **F)** Psb32-PSII and mature PSII (grey). In **D-F** residues that coordinate the Mn_4O_5Ca cluster in the mature state are highlighted. In **B** and **E**, arrows indicate major conformational changes between Psb27-PSII and Psb32-PSII. Density fitting of the shown residues is illustrated in Fig. S13.

Discussion

In our study we were able to elucidate the structure and function of the Psb32-PSII assembly intermediate. Our findings indicate that the assembly factor Psb32 interacts with the extrinsic subunit PsbV and with Psb27, a prominent factor previously described to facilitate the attachment of the CP43 antenna

273 module to RC47[10,13,14]. The tail-anchored protein Psb32 is comprised of two major functional parts, and
274 we hypothesize that they fulfill distinct roles within the assembly complex.

275 The C-terminal transmembrane helix of Psb32 binds near Cyt b_{559} and occupies the same position as
276 PsbY in the mature complex. Although the overall induced changes to the coordination of Cyt b_{559} are
277 neglectable within the error of resolution, Psb32 may influence its redox properties. This is of im-
278 portance because Cyt b_{559} can switch between four redox forms (high potential: Em of +370–400 mV;
279 intermediate potential: Em + 170–250 mV; low potential: Em + 70–100 mV; very low potential: Em
280 −45 mV) but the structural origin for this redox-switching mechanism is still unknown[29]. The high po-
281 tential (HP) form is characterized by an at least temporarily reduced heme iron, which can't be oxidized
282 by oxygen. Therefore, it can serve as an alternative electron donor for P680+. Instead, all low potential
283 forms of Cyt b_{559} can be easily oxidized by oxygen and thus have the capability to accept an electron
284 from the PSII acceptor side. By switching between the HP and LP form, Cyt b_{559} is involved in photo-
285 protection by providing cyclic electron flow between the PSII acceptor and donor side[30,31]. This protec-
286 tion mechanism operates in PSII complexes without a functional OEC and has been shown to be im-
287 portant for its photoactivation[32]. Moreover, Cyt b_{559} of PSII without PsbY is also locked in the low
288 potential state but little is known about the mechanism by which it switches between the two states[33].

289 The lumenal domain of Psb32 is mainly coordinated by PsbV and Psb27 and may facilitate its attach-
290 ment to the PSII complex. This is an unexpected finding, since the last steps, the association of the
291 extrinsic subunits, were thought to be a spontaneous and unassisted process based on *in vitro* experi-
292 ments[34]. In the cell, the situation may be different, and Psb32 can control the direction of the process
293 and improve the efficiency of the assembly process. Based on our structure, a possible scenario might
294 be that Psb32 stabilizes the binding of PsbV, which in turn is necessary to recruit PsbO to the complex
295 in the next step to flip the D2 C-terminus into the mature position. This would explain why PsbO is not
296 bound to any intermediate complex until the Mn_4O_5Ca cluster is integrated.

297 Furthermore, the above considerations for the role of Psb32 in PSII assembly are also consistent with
298 its predicted role within the repair cycle[18], as the reassembly of damaged complexes overlaps with the
299 stages of *de novo* biogenesis described above[7]. Psb32 was shown to be associated with active PSII,

300 protecting the complex from peroxide[18,35,36]which may be related to its influence on Cyt b_{559} in Psb32-
301 PSII. Besides the protection mechanism, it might be possible that binding of Psb27 is increased in pres-
302 ence of Psb32, initiating repair by anchoring Psb27. This suggests that Psb32 may play a role in recruit-
303 ing Psb27, in addition to its involvement in assembly. This could provide an alternative explanation for
304 the reduced PSII recovery rates observed in a Psb32 deletion strain following photoinhibition by high
305 light[18].

306 By integrating these new findings, we can now extend the existing model of the PSII assembly (Figure 6).
307 Following the formation of the reaction center complex (RCC), a pre-module consisting of CP47 and
308 several low molecular weight proteins (LMWPs) attaches, resulting in the formation of RC47. This
309 complex is stabilized by the action of Psb28 and Psb34 that induces significant structural alterations on
310 the acceptor side of PSII that prevent binding of bicarbonate (BIC) to the non-heme iron. This may shift
311 the Q_A/Q_A- redox potential to a more positive value to promote safe charge recombination[10,37], which
312 protects the immature complex from oxidative damage. Subsequently, RC47 associates with the CP43
313 module. Previous work demonstrated that Psb27 is already bound to free CP43, where it might protect
314 free CP43 from degradation or maintaining the E-loop in a conformation suitable for its subsequent
315 association with the RC47 complex[13,27]. The structure of the resulting assembly intermediate revealed
316 how a not-yet-completely assembled but already partially active molecular machine is protected from
317 photodamage[10,14]. In this intermediate the Q_B site is not matured. However, our new structures show that
318 following the dissociation of Psb28 and Psb34 and the binding of PsbJ, the Q_B site matures, with a
319 molecule of PQ bound, similar to mature PSII. This maturation is a prerequisite for forward electron
320 flow[15]. Apart from the binding of extrinsic subunits, this complex now seems to be intact. However,
321 there are still side chains around the OEC that are not yet in a mature conformation, verifying that Psb27
322 on its own is not sufficient to promote photoactivation. Upon maturation of the acceptor side, Psb32
323 binds to the complex and, interestingly, the coordination site progresses towards maturation, as indicated
324 by the conformational shifts in His332 and Glu333. These key residues are now in their final position
325 to coordinate the Mn_4O_5Ca cluster, suggesting that Psb32, along with PsbV, plays a crucial role in ini-
326 tiating these transitions. All in all, the structural transitions underline the role of both Psb32 and PsbV
327 in the final steps of PSII assembly. Furthermore, the critical role of PsbO in photoactivation becomes

increasingly clear, though its action relies on a well-prepared environment orchestrated by the other biogenesis factors. Following photoactivation, Psb32 is replaced by PsbY, a shift that promotes forward electron transfer over cyclic electron transfer via Cyt b_{559} that offered protection against photoinhibition in the yet inactive complex.

With this research, we now have a comprehensive understanding of the final steps in the PSII biogenesis and assembly pipeline, with only PsbY and the extrinsic subunits PsbO and PsbU remaining to be incorporated.

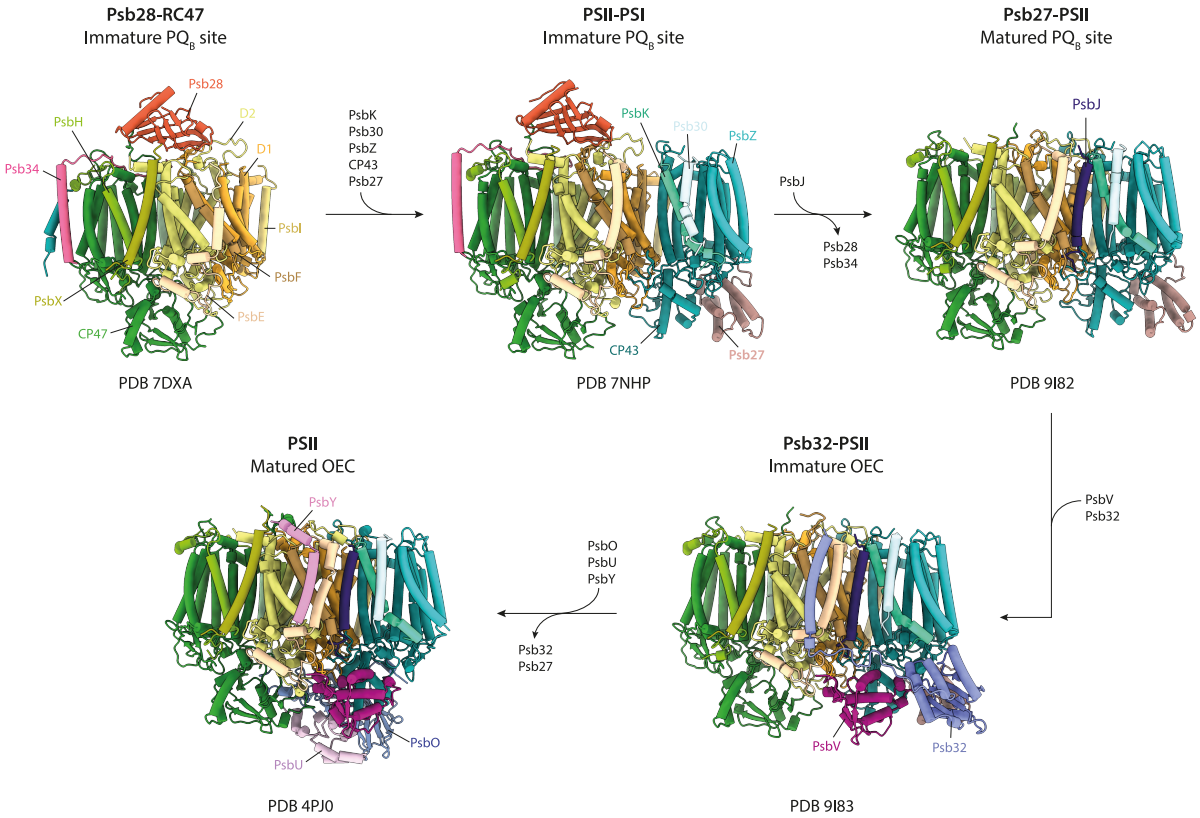

Figure 6: Schematic model of the late PSII assembly process after formation of Psb28-RC47. Association of the CP43 module to RC47 is stabilized by the assembly factor Psb27. Upon binding of the LMWP PsbJ, Psb28 and Psb34 are released from Psb27-PSII, forming the matured PQ_B site. Psb32 aids the assembly of the extrinsic subunit PsbV. Additionally, Psb32 prevents binding of PsbY, thus possibly protecting the immature intermediate from redox damage. Maturation of PSII is followed by association of the remaining subunits, as well as release of Psb32 and Psb27.

Material and methods

Mutant generation and cultivation

A *Thermosynechococcus vestitus* BP-1 mutant line was created by modifying the N-terminal sequence of Psb27 with a Twin-Strep-Tag after the N-terminal Cysteine (Sequence: C_{mod}ANV-GGGSSAW-SHPQFEKGGGGSSGGGSAWSHPQFEKGGGS-Psb27). The DNA-sequence was synthesized by Twist Bioscience (USA) and transferred into the pJET1.2 vector with the CloneJET PRC-cloning kit according to the manufacturer (Thermo Fisher Scientific). A restriction site was integrated 170 bp upstream of Psb27, in which a kanamycin resistance cassette was integrated by ligation. Segregation was confirmed by PCR using forward (GAGCGATATCCATCCACGGTTGCCAAGAG) and reverse (GCCGAATTCTACCCTAACCCGCTGCTGTC) primers binding before and after the resistance cassette, respectively. The strain was grown in 25-L photobioreactors (Bioengineering) in Bg-11 media using in presence of 150 $\mu g \cdot ml^{-1}$ kanamycin[28]. The cells were harvested, pelleted and the membranes extracted with a parr bomb as described previously[28].

Protein purification

PSII complexes were extracted from thylakoid membranes and purified by Strep-tag affinity chromatography as described previously using Strep-Tactin®XT® columns (IBA Lifesciences)[38]. The final buffer of the protein complexes was PSII-DDM-buffer (20 mM MES pH 6.5, 10 mM $CaCl_2$, 10 mM $MgCl_2$, 500 mM mannitol with 0.03% (w/v) n-dodecyl-ß-d-maltoside (DDM)).

Detergent-exchange and removal

In scope of the cryo-EM sample preparation we exchanged the detergent DDM to lauryl maltose neopentyl glycol (LMNG) directly on Strep-Tactin®XT® columns (CV = 5 ml). The sample was applied to the column in PSII-DDM-buffer, which was was exchanged to PSII-LMNG-buffer (PSII-buffer with 0.05% (w/v) LMNG) in a gradient from 20% to 100% over 8 CV. After full removal of the PSII-DDM-buffer (after 1 CV 100% PSII-LMNG-buffer), a second gradient from 80% to 0% PSII-LMNG-buffer against a detergent-free PSII-buffer was done over 6 CV. Proteins were eluted with 50 mM biotin in

370 PSII-buffer without detergent after 1 CV of washing at 100% PSII-buffer without detergent. During all
371 steps, a flow rate of 1 ml·min^{-1} was applied.

372 Biochemical characterization

373 Oxygen evolution measurements were done as described previously[28] with isolated protein equal to 2-5
374 µg·ml^{-1} Chl in presence of 1 mM 2,6-Dichloro-1,4-benzoquinone (DCBQ) and 5 mM ferricyanide. Blue-
375 native PAGE and urea-based SDS-PAGE were done as described previously[39,40]. As size standard, Ther-
376 mofisher PageRuler Prestained protein ladder #26616 or purified PSII[38] were applied.

377 MALDI-ToF MS

378 MALDI-ToF MS measurements were performed as described by[38]. Briefly, the target subunits were
379 purified using C18-ZipTips (Merck, Germany). The eluted organic fractions were lyophilized in a vac-
380 uum concentrator (Eppendorf, Germany), reconstituted in 0.1% Trifluoroacetic acid (TFA) and mixed
381 in a 1:1 ratio with sDHB (Bruker Daltonics, Germany) matrix solution (50 mg/ml in 50% (v/v) Acetoni-
382 trile (ACN), 50% (v/v) water and 0.1% (v/v) TFA). Subsequently 1 µl aliquots of the mixture were
383 deposited on a BigAnchor MALDI target (Bruker Daltonics, Germany) and allowed to dry and crystal-
384 lize at ambient conditions.

385 MS spectra were acquired on a rapifleX MALDI-TOF/TOF (Bruker Daltonics, Germany) in the mass
386 range from 3000-7000 m/z in reflector positive mode. The Compass 2.0 (Bruker, Germany) software
387 suite was used for spectra acquisition and processing.

388

389 LC-MS

390 Protein samples were reduced with TCEP and cysteines alkylated with IAA (Thermo Fisher, Germany).
391 Subsequent proteolytic digests were performed using S-TRAPs (Protifi, USA) according to the manu-
392 facturer's instructions. Peptides were further desalted and purified on Isolute C18 SPE cartridges (Bio-
393 tage, Sweden) and dried in an Eppendorf concentrator (Eppendorf, Germany) as described by[10]. After
394 solubilization in 0.1% (v/v) formic acid (FA) in ACN/water (95/5, v/v), samples were subjected to LC-
395 MS/MS analysis on a nanoElute (Bruker, Germany) system, equipped with C18 analytical column (15

396 cm * 75 µm, particle size: 1.9 µm (PepSep, Denmark)) coupled to a timsTOF Pro 2 mass spectrometer
397 (Bruker, Germany). Samples were loaded directly onto the analytical column with twice the sample
398 pick-up volume with buffer A. Peptides were separated on the analytical column at a flow rate of 500
399 nl/min with the following gradient: 2 to 35% B in 17.8 min, 35 to 95% B in 0.5 min and constant 90 %
400 B for 2.4 min with buffer A (0.1% FA in water) and buffer B (0.1% FA in acetonitrile). Peptides eluting
401 from the column were ionized online using a captive spray ion-source and analyzed in DDA-PASEF
402 mode with a cycle time of 100 ms and 4 PASEF-MS/MS events. Spectra were acquired over the mass
403 range from 100-1700 m/z and a mobility window from 0.85-1.3 Vs/cm^2.

404 Data analysis was performed in Fragpipe 17.1 using MSFragger 3.4 for database searches[41]. Raw files
405 were recalibrated and searched against the Uniprot proteome for *Thermosynechococcus vestitus*
406 (UP000000440; obtained 2022-03-17) along with the modified Psb27 sequence. The search space was
407 restricted to tryptic peptides with a length of 7-50 amino acids, allowing for up to two missed cleavages
408 and with a minimum of one unique peptide per protein group. Carbamidomethylation of Cysteine was
409 set as a fixed modification and oxidation of Methionine as well as N-terminal formylation and acetyla-
410 tion were set as variable modification. Percolator was used to estimate the number of false positive
411 identifications and the results were filtered for a strict target false discovery rate (FDR) < 0.01.

412 The mass spectrometry proteomics data have been deposited to the ProteomeXchange Consortium
413 (http://proteomecentral.proteomexchange.org) via the PRIDE partner repository[42] with the dataset iden-
414 tifier PXD061441.

415

416 **Cryo-electron microscopy**

417 For cryo-EM sample preparation, 4.5µl of the purified complex were applied to glow discharged Quan-
418 tifoil 2/1 grids, blotted for 3.5s with force 4 in a Vitrobot Mark III (Thermo Fisher) at 100% humidity
419 and 4°C, and plunge frozen in liquid ethane, cooled by liquid nitrogen. Cryo-EM data was acquired with
420 an FEI Titan Krios transmission electron microscope using SerialEM software[43]. Movie frames were
421 recorded at a nominal magnification of 29,000X using a K3 direct electron detector (Gatan). The total

422 electron dose of ~55 electrons per $Å^2$ was distributed over 30 frames at a calibrated physical pixel size
423 of 0.84 Å. Micrographs were recorded in a defocus range of -0.5 to -3.0 µm.

424

425 Image processing, classification, and refinement

426 Cryo-EM micrographs of PSII isolated by TS-Psb27 were processed on the fly using the Focus software
427 package[44] if they passed the selection criteria (iciness < 1.05, drift 0.4 Å < x < 70 Å, defocus 0.5 µm <
428 x < 5.5 µm, estimated CTF resolution < 6 Å). Micrograph frames were aligned using MotionCor2[45] and
429 the contrast transfer function (CTF) for aligned frames was determined using GCTF[46]. From 20,182
430 acquired micrographs 5,055,941 particles were picked using the Phosaurus neural network architecture
431 from crYOLO[47]. Particles were extracted with a pixel box size of 256 scaled down to 64 using RELION
432 3.1[48] and underwent several rounds of reference-free 2D classification At this stage, obvious non-parti-
433 cles (carbon edges, contamination, overlapping particles) and views that failed to align coherently were
434 removed, as these species do not contribute meaningful signal and would otherwise reduce the resolution
435 of downstream reconstructions. The remaining 3,100,431 selected particles were re-extracted with a box
436 size of 320 and imported into Cryosparc 2.3[49], given its GPU-accelerated algorithms enable substantially
437 faster exploration of structural heterogeneity, an advantage when handling millions of particles and mul-
438 tiple potential intermediate states. After *ab initio* model generation and heterogeneous refinement parti-
439 cles of the Psb32-PSII like class were re-imported to RELION and further classified in 2D. Poorly
440 aligned particles that did not contribute to meaningful reconstruction were discarded. Selected particles
441 were down-sampled to a box size of 128 and refined against a consensus model. Using 3D focused
442 classification without alignment gave rise to distinct classes with (199,653 particles) and without Psb32
443 (325,601), while discarding residual heterogeneous particles that did not converge to defined densities.
444 Several rounds of refinement, CTF-refinement (estimation of anisotropic magnification, fit of per-mi-
445 crograph defocus and astigmatism and beam tilt estimation) and Bayesian polishing[50] yielded final mod-
446 els with an estimated resolution of ~2.9 Å and ~2.8 Å for PSII with Psb32 and without Psb32, respec-
447 tively (Gold standard FSC analysis of two independent half-sets at the 0.143 cutoff). Local-resolution

448 and 3D-FSC plots (Figure S3) were calculated using RELION and the "Remote 3DFSC Processing
449 Server" web interface[51], respectively.

450

451 **Atomic model construction**

452 The 3.6 Å resolution X-ray crystal structure of monomeric PSII from *T. vestitus* with PDB-ID 3KZI[52]
453 was used as initial structural model that was docked as rigid body using Chimera[53] into the obtained
454 cryo-EM density maps of Psb32-PSII and Psb27-PSII. For all PSII complexes, the subunits and cofac-
455 tors that had no corresponding density were removed. By highlighting the still unoccupied parts of the
456 density maps, we identified the density regions that belong to subunits of the PSII that are not present
457 in the initial structure and therefore need to be added to the model. For Psb32-PSII we assigned the
458 unoccupied densities to the mass spectrometry identified subunits Psb27 and Psb32. For Psb27-PSII we
459 assigned Psb27. For Psb32-PSII we deleted PsbO and PsbU from the initial structural model and for
460 Psb27-PSII we deleted PsbO, PsbU, and PsbV. The 1.6 Å resolution X-ray crystal structure of isolated
461 Psb27 from *T. vestitus* with PDB-ID 2Y6X[54] was docked as rigid body into the unoccupied density
462 assigned to Psb27 in all three complexes.

463 We first determined the atomic structure of isolated mature Psb32 (UniProt ID Q8DLS4) with a fused
464 sfGFP at the N-terminus using X-ray crystallography based on data obtained earlier[55]. The initial model
465 after determination of phases by BALBES[56] was further refined using Phenix[57] and Coot[58] against the
466 native dataset with a resolution of 2.12 Å. Refinement included individual B-factors and TLS refinement
467 using TLS groups automatically defined by Phenix. Residues 0 to150 of the deposited coordinates
468 (PDB-ID 8C7I), which correspond to the residues 30 to 180 in the Uniprot entry Q8DLS4, were then
469 used for docking into the previously assigned cryo-EM density. Interestingly, there was still unoccupied
470 density left reflecting the truncated C-terminal tail of Psb32 that could not be resolved by X-ray crystal-
471 lography due to its high flexibility in the isolated form.

472 We predicted models of the complete Psb32 sequence (UniProt ID Q8DLS4) using AlphaFold2[59] and
473 AlphaFold3[60]. We also predicted the secondary structure through the meta server Bioinformatics

474 Toolkit[61] and CCTOP[62]. All results provide an almost identical length of the C-terminal α-helix. There-
475 fore, we merged the C-terminus from residue 181 to 228 of the AlphaFold3 predicted model with the
476 docked Psb32 X-ray crystal structure. Then, we performed interactive molecular dynamics flexible fit-
477 ting (MDFF) to fit the C-terminus into the identified unoccupied density.

478

479 Model Refinement

480 Our employed model refinement strategy is well established and was applied to construct structural
481 models of several different complex molecular machines by employing different bioinformatics protein
482 modelling and simulation methods to interpret cryo-EM. The initial model of the complexes described
483 above were refined in real space against the respective cryo-EM density, and structural clashes were
484 removed using MDFF[63]. MDFF simulations were prepared in VMD 1.9.4a35[64] using QwikMD[65] and
485 the MDFF plugin. The simulations were carried out with NAMD 2.13[66] employing the CHARMM36
486 force field. Secondary structure, cis peptide and chirality restraints were employed during 800 steps of
487 minimization followed by a 40 ps MDFF simulation at 300K. Due to the employed restraints, only
488 conformational changes of side chains and subunit movements compared to the initial structure are iden-
489 tified during the initial MDFF run. We checked the fit to density of the structure by calculating cross-
490 correlation values of the backbone atoms.

491 After the initial MDFF runs, the cross-correlation check did not reveal any regions with significant de-
492 viation between model and density. Therefore, no further refinement of secondary structure elements
493 was necessary. This fast convergence reflects that there are no large conformational differences between
494 the model and the initial X-ray crystal structures, except for the presence of the further subunits. Then,
495 all three models were used to initiate one final round of real-space refinement in Phenix[57]. Last, a final
496 inspection of steric clashes and chemical correctness e.g. of side chain head group orientations is per-
497 formed using the prepare and inspect algorithms implemented in MAXIMOBY (CHEOPS, Germany).

498

Structure Analysis

The atomic interaction pattern between the subunits were identified and analyzed using the MAXI-MOBY (CHEOPS, Germany) contact matrix algorithm and the VMD plugin PyContact[67]. Structural difference between structures were identified and highlighted through calculation of the residue wise root mean square deviation of the backbone Cα atoms.

Phylogenetic Analysis

For the phylogenetic analysis, Psb32 and Psb32-like sequences from Streptophyta, Chlorophyta, Cyanobacteria and Bacteria were collected from the NCBI database (June 2024) using BLAST. Sequences were aligned with MAFFT 7.110 using the iterative refinement method with global pairwise alignment information (G-INS-i) and an offset value (gap extension penalty) of 2. Cyanobacteria encode a second psb32-like paralog with a long insertion near the C-terminus. These sequences were aligned separately and then combined with the other sequences in a profile alignment using the merge function of MAFFT. The resulting alignment was manually curated by removing lineage-specific insertions.

A maximum likelihood phylogeny was inferred using IQ-TREE 2.0.3. Using ModelFinder restricted to nuclear amino acid models the best fit was determined to be the general matrix WAG with empirical amino acid frequencies, a proportion of invariable sites, and the discrete gamma model with 4 rate categories to account for rate heterogeneity across sites (WAG+F+I+G4). The resulting tree was rooted with sequences from Margulisbacteria which form a distinct and monophyletic outgroup. Standard non-parametric (Felsenstein) bootstraps were calculated in 100 replicates using IQ-TREE 2.0.3 to assess the robustness of the phylogenetic inference.

References

1. Shen, J.-R. The Structure of Photosystem II and the Mechanism of Water Oxidation in Photosynthesis. *Annu. Rev. Plant Biol.* **66,** 23–48; 10.1146/annurev-arplant-050312-120129 (2015).
2. Umena, Y., Kawakami, K., Shen, J.-R. & Kamiya, N. Crystal structure of oxygen-evolving photosystem II at a resolution of 1.9 Å. *Nature* **473,** 55–60; 10.1038/nature09913 (2011).
3. Shi, L.-X., Hall, M., Funk, C. & Schröder, W. P. Photosystem II, a growing complex: updates on newly discovered components and low molecular mass proteins. *Biochimica et Biophysica Acta (BBA)* **1817,** 13–25; 10.1016/j.bbabio.2011.08.008 (2012).
4. Lubitz, W., Pantazis, D. A. & Cox, N. Water oxidation in oxygenic photosynthesis studied by magnetic resonance techniques. *FEBS Letters* **597,** 6–29; 10.1002/1873-3468.14543 (2023).
5. Cox, N., Pantazis, D. A. & Lubitz, W. Current Understanding of the Mechanism of Water Oxidation in Photosystem II and Its Relation to XFEL Data. *Annual review of biochemistry* **89,** 795–820; 10.1146/annurev-biochem-011520-104801 (2020).
6. Roose, J. L., Frankel, L. K., Mummadisetti, M. P. & Bricker, T. M. The extrinsic proteins of photosystem II: update. *Planta* **243,** 889–908; 10.1007/s00425-015-2462-6 (2016).
7. Johnson, V. M. & Pakrasi, H. B. Advances in the Understanding of the Lifecycle of Photosystem II. *Microorganisms* **10,** 836; 10.3390/microorganisms10050836 (2022).
8. Komenda, J., Sobotka, R. & Nixon, P. J. The biogenesis and maintenance of PSII: Recent advances and current challenges. *Plant Cell* **36,** 3997–4013; 10.1093/plcell/koae082 (2024).
9. Heinz, S., Liauw, P., Nickelsen, J. & Nowaczyk, M. Analysis of photosystem II biogenesis in cyanobacteria. *Biochimica et Biophysica Acta (BBA)* **1857,** 274–287; 10.1016/j.bbabio.2015.11.007 (2016).
10. Zabret, J. *et al.* Structural insights into photosystem II assembly. *Nat. Plants* **7,** 524–538; 10.1038/s41477-021-00895-0 (2021).
11. Nowaczyk, M. M. *et al.* Psb27, a cyanobacterial lipoprotein, is involved in the repair cycle of photosystem II. *The Plant cell* **18,** 3121–3131; 10.1105/tpc.106.042671 (2006).
12. Roose, J. L. & Pakrasi, H. B. The Psb27 protein facilitates manganese cluster assembly in photosystem II. *The Journal of Biological Chemistry* **283,** 4044–4050; 10.1074/jbc.M708960200 (2008).
13. Komenda, J. *et al.* The Psb27 assembly factor binds to the CP43 complex of photosystem II in the cyanobacterium *Synechocystis* sp. PCC 6803. *Plant physiology* **158,** 476–486; 10.1104/pp.111.184184 (2012).
14. Xiao, Y. *et al.* Structural insights into cyanobacterial photosystem II intermediates associated with Psb28 and Tsl0063. *Nat. Plants* **7,** 1132–1142; 10.1038/s41477-021-00961-7 (2021).
15. Bao, H. & Burnap, R. L. Photoactivation: The Light-Driven Assembly of the Water Oxidation Complex of Photosystem II. *Frontiers in plant science* **7,** 578; 10.3389/fpls.2016.00578 (2016).
16. Sirpiö, S. *et al.* TLP18.3, a novel thylakoid lumen protein regulating photosystem II repair cycle. *The Biochemical journal* **406,** 415–425; 10.1042/BJ20070460 (2007).
17. Wegener, K. M. *et al.* High sensitivity proteomics assisted discovery of a novel operon involved in the assembly of photosystem II, a membrane protein complex. *Journal of Biological Chemistry* **283,** 27829–27837; 10.1074/jbc.M803918200 (2008).
18. Wegener, K. M., Bennewitz, S., Oelmüller, R. & Pakrasi, H. B. The Psb32 protein aids in repairing photodamaged photosystem II in the cyanobacterium *Synechocystis* 6803. *Molecular plant* **4,** 1052–1061; 10.1093/mp/ssr044 (2011).
19. Wu, H.-Y., Liu, M.-S., Lin, T.-P. & Cheng, Y.-S. Structural and functional assays of AtTLP18.3 identify its novel acid phosphatase activity in thylakoid lumen. *Plant Physiol* **157,** 1015–1025; 10.1104/pp.111.184739 (2011).
20. Spetea, C. & Lundin, B. Evidence for nucleotide-dependent processes in the thylakoid lumen of plant chloroplasts - an update. *FEBS Letters* **586,** 2946–2954; 10.1016/j.febslet.2012.07.005 (2012).

21. Breyton, C. *et al.* Assemblies of lauryl maltose neopentyl glycol (LMNG) and LMNG-solubilized membrane proteins. *Biochimica et Biophysica Acta (BBA) - Biomembranes* **1861,** 939–957; 10.1016/j.bbamem.2019.02.003 (2019).

22. Gisriel, C. J. *et al.* Cryo-EM Structure of Monomeric Photosystem II from *Synechocystis* sp. PCC 6803 Lacking the Water-Oxidation Complex. *Joule* **4,** 2131–2148; 10.1016/j.joule.2020.07.016 (2020).

23. Huang, G. *et al.* Structural insights into a dimeric Psb27-photosystem II complex from a cyanobacterium *Thermosynechococcus vulcanus*. *PNAS* **118,** e2018053118; 10.1073/pnas.2018053118 (2021).

24. Hellmich, J. *et al.* Native-like photosystem II superstructure at 2.44 Å resolution through detergent extraction from the protein crystal. *Structure (London, England : 1993)* **22,** 1607–1615; 10.1016/j.str.2014.09.007 (2014).

25. Shinopoulos, K. E. & Brudvig, G. W. Cytochrome b_{559} and cyclic electron transfer within photosystem II. *Biochimica et biophysica acta* **1817,** 66–75; 10.1016/j.bbabio.2011.08.002 (2012).

26. Rühle, T. & Leister, D. Photosystem II Assembly from Scratch. *Frontiers in plant science* **6,** 1234; 10.3389/fpls.2015.01234 (2015).

27. Liu, H., Huang, R. Y.-C., Chen, J., Gross, M. L. & Pakrasi, H. B. Psb27, a transiently associated protein, binds to the chlorophyll binding protein CP43 in photosystem II assembly intermediates. *Proceedings of the National Academy of Sciences of the United States of America* **108,** 18536–18541; 10.1073/pnas.1111597108 (2011).

28. Lambertz, J., Liauw, P., Whitelegge, J. P. & Nowaczyk, M. M. Mass spectrometry analysis of the photosystem II assembly factor Psb27 revealed variations in its lipid modification. *Photosynth Res,* Available online under https://doi.org/10.1007/s11120-021-00891-7; 10.1007/s11120-021-00891-7 (2021).

29. Pospíšil, P. Enzymatic function of cytochrome *b*559 in photosystem II. *Journal of photochemistry and photobiology. B, Biology* **104,** 341–347; 10.1016/j.jphotobiol.2011.02.013 (2011).

30. Barber, J. & Las Rivas, J. de. A functional model for the role of cytochrome b559 in the protection against donor and acceptor side photoinhibition. *Proceedings of the National Academy of Sciences* **90,** 10942–10946; 10.1073/pnas.90.23.10942 (1993).

31. Thompson, L. K. & Brudvig, G. W. Cytochrome b-559 may function to protect photosystem II from photoinhibition. *BIOCHEM.J.* **27,** 6653–6658; 10.1021/bi00418a002 (1988).

32. Mizusawa, N., Miyao, M. & Yamashita, T. Restoration of the high-potential form of cytochrome b-559 by electron transport reactions through Photosystem II in Tris-treated Photosystem II membranes. *Biochimica et Biophysica Acta (BBA) - Bioenergetics* **1318,** 145–158; 10.1016/S0005-2728(96)00130-2 (1997).

33. von Sydow, L. *et al.* The PsbY protein of *Arabidopsis* Photosystem II is important for the redox control of cytochrome b_{559}. *Biochimica et Biophysica Acta (BBA)* **1857,** 1524–1533; 10.1016/j.bbabio.2016.05.004 (2016).

34. Shen, J. R. & Inoue, Y. Binding and functional properties of two new extrinsic components, cytochrome c_{550} and a 12-kDa protein, in cyanobacterial photosystem II. *Biochemistry* **32,** 1825–1832; 10.1021/bi00058a017 (1993).

35. Kashino, Y. *et al.* Proteomic analysis of a highly active photosystem II preparation from the cyanobacterium *Synechocystis* sp. PCC 6803 reveals the presence of novel polypeptides. *Biochemistry* **41,** 8004–8012; 10.1021/bi026012 (2002).

36. Dahlgren, K. K., Gates, C., Lee, T. & Cameron, J. C. Proximity-based proteomics reveals the thylakoid lumen proteome in the cyanobacterium *Synechococcus* sp. PCC 7002. *Photosynth Res* **147,** 177–195; 10.1007/s11120-020-00806-y (2021).

37. Brinkert, K., De Causmaecker, S., Krieger-Liszkay, A., Fantuzzi, A. & Rutherford, A. W. Bicarbonate-induced redox tuning in Photosystem II for regulation and protection. *Proceedings of the National Academy of Sciences* **113,** 12144–12149; 10.1073/pnas.1608862113 (2016).

38. Lambertz, J. *et al.* Isolation of a novel heterodimeric PSII complex via strep-tagged PsbO **bioRxiv,** https://www.biorxiv.org/content/10.1101/2022.06.15.496312v1.full; 10.1101/2022.06.15.496312 (2022).

39. Schägger, H. & Jagow, G. von. Tricine-sodium dodecyl sulfate-polyacrylamide gel electrophoresis for the separation of proteins in the range from 1 to 100 kDa. *Analytical biochemistry* **166,** 368–379; 10.1016/0003-2697(87)90587-2 (1987).

40. Schägger, H. & Jagow, G. von. Blue native electrophoresis for isolation of membrane protein complexes in enzymatically active form. *Analytical biochemistry* **199,** 223–231; 10.1016/0003-2697(91)90094-A (1991).

41. Kong, A. T., Leprevost, F. V., Avtonomov, D. M., Mellacheruvu, D. & Nesvizhskii, A. I. MSFragger: ultrafast and comprehensive peptide identification in mass spectrometry-based proteomics. *Nat Methods* **14,** 513–520; 10.1038/nmeth.4256 (2017).

42. Perez-Riverol, Y. *et al.* The PRIDE database and related tools and resources in 2019: improving support for quantification data. *Nucleic Acids Res* **47,** D442-D450; 10.1093/nar/gky1106 (2019).

43. Mastronarde, D. N. Automated electron microscope tomography using robust prediction of specimen movements. *Journal of structural biology* **152,** 36–51; 10.1016/j.jsb.2005.07.007 (2005).

44. Biyani, N. *et al.* Focus: The interface between data collection and data processing in cryo-EM. *Journal of structural biology* **198,** 124–133; 10.1016/j.jsb.2017.03.007 (2017).

45. Zheng, S. Q. *et al.* MotionCor2: anisotropic correction of beam-induced motion for improved cryo-electron microscopy. *Nat Methods* **14,** 331–332; 10.1038/nmeth.4193 (2017).

46. Zhang, K. Gctf: Real-time CTF determination and correction. *Journal of structural biology* **193,** 1–12; 10.1016/j.jsb.2015.11.003 (2016).

47. Wagner, T. *et al.* SPHIRE-crYOLO is a fast and accurate fully automated particle picker for cryo-EM. *Commun Biol* **2,** 218; 10.1038/s42003-019-0437-z (2019).

48. Scheres, S. H. W. A Bayesian view on cryo-EM structure determination. *Journal of molecular biology* **415,** 406–418; 10.1016/j.jmb.2011.11.010 (2012).

49. Punjani, A., Rubinstein, J. L., Fleet, D. J. & Brubaker, M. A. cryoSPARC: algorithms for rapid unsupervised cryo-EM structure determination. *Nat Methods* **14,** 290–296; 10.1038/nmeth.4169 (2017).

50. Scheres, S. H. Beam-induced motion correction for sub-megadalton cryo-EM particles. *eLife* **3,** e03665; 10.7554/eLife.03665 (2014).

51. Tan, Y. Z. *et al.* Addressing preferred specimen orientation in single-particle cryo-EM through tilting. *Nat Methods* **14,** 793–796; 10.1038/nmeth.4347 (2017).

52. Broser, M. *et al.* Crystal structure of monomeric photosystem II from Thermosynechococcus elongatus at 3.6-a resolution. *Journal of Biological Chemistry* **285,** 26255–26262; 10.1074/jbc.M110.127589 (2010).

53. Pettersen, E. F. *et al.* UCSF Chimera--a visualization system for exploratory research and analysis. *Journal of computational chemistry* **25,** 1605–1612; 10.1002/jcc.20084 (2004).

54. Michoux, F. *et al.* Crystal structure of the Psb27 assembly factor at 1.6 Å: implications for binding to Photosystem II. *Photosynth Res* **110,** 169–175; 10.1007/s11120-011-9712-7 (2012).

55. Liauw, P. *et al.* Cloning, expression, crystallization and preliminary X-ray studies of a superfolder GFP fusion of cyanobacterial Psb32. *Acta crystallographica. Section F, Structural biology communications* **71,** 409–413; 10.1107/S2053230X15003970 (2015).

56. Long, F., Vagin, A. A., Young, P. & Murshudov, G. N. BALBES: a molecular-replacement pipeline. *Acta Cryst D* **64,** 125–132; 10.1107/S0907444907050172 (2008).

57. Liebschner, D. *et al.* Macromolecular structure determination using X-rays, neutrons and electrons: recent developments in Phenix. *Acta crystallographica. Section D, Structural biology* **75,** 861–877; 10.1107/S2059798319011471 (2019).

58. Emsley, P., Lohkamp, B., Scott, W. G. & Cowtan, K. Features and development of Coot. *Acta crystallographica. Section D, Biological crystallography* **66,** 486–501; 10.1107/S0907444910007493 (2010).

59. Jumper, J. *et al.* Highly accurate protein structure prediction with AlphaFold. *Nature* **596,** 583–589; 10.1038/s41586-021-03819-2 (2021).

60. Abramson, J. *et al.* Accurate structure prediction of biomolecular interactions with AlphaFold 3. *Nature* **630,** 493–500; 10.1038/s41586-024-07487-w (2024).

61. Zimmermann, L. *et al.* A Completely Reimplemented MPI Bioinformatics Toolkit with a New HHpred Server at its Core. *Journal of molecular biology* **430,** 2237–2243; 10.1016/j.jmb.2017.12.007 (2018).

62. Dobson, L., Reményi, I. & Tusnády, G. E. CCTOP: a Consensus Constrained TOPology prediction web server. *Nucleic Acids Res* **43,** W408-12; 10.1093/nar/gkv451 (2015).

63. Trabuco, L. G., Villa, E., Schreiner, E., Harrison, C. B. & Schulten, K. Molecular dynamics flexible fitting: a practical guide to combine cryo-electron microscopy and X-ray crystallography. *Methods (San Diego, Calif.)* **49,** 174–180; 10.1016/j.ymeth.2009.04.005 (2009).

64. Humphrey, W., Dalke, A. & Schulten, K. VMD: Visual molecular dynamics. *Journal of Molecular Graphics* **14,** 33–38; 10.1016/0263-7855(96)00018-5 (1996).

65. Ribeiro, J. V. *et al.* QwikMD - Integrative Molecular Dynamics Toolkit for Novices and Experts. *Sci Rep* **6,** 26536; 10.1038/srep26536 (2016).

66. Phillips, J. C. *et al.* Scalable molecular dynamics with NAMD. *Journal of computational chemistry* **26,** 1781–1802; 10.1002/jcc.20289 (2005).

67. Scheurer, M. *et al.* PyContact: Rapid, Customizable, and Visual Analysis of Noncovalent Interactions in MD Simulations. *Biophysical Journal* **114,** 577–583; 10.1016/j.bpj.2017.12.003 (2018).

Structural insights into late-stage photosystem II assembly by Psb32

Stefan Bohn[#1], Yat Kei Lo[#2], Jan Lambertz[#3], Jakob Meier-Credo[4], Torben Fürtges[5], Pasqual Liauw[3], Raphael Gasper-Schönenbrücher[6], Dennis Wiens[7], Julian D. Langer[4,8], Georg Hochberg[7], Eckhard Hofmann[6], Till Rudack[*5], Marc M. Nowaczyk[*3,9,10], Jan M. Schuller[*2]

# These authors contributed equally

* Corresponding authors

Email: marc.m.nowaczyk@uni-rostock.de; till.rudack@ur.de; jan.schuller@synmikro.uni-marburg.de

1 Helmholtz Zentrum München, Institute of Structural Biology, Ingolstädter Landstraße 1, 85764 Neuherberg, Germany

2 CryoEM of Molecular Machines, SYNMIKRO Research Center and Department of Chemistry, Philipps University of Marburg, Marburg, Germany

3 Plant Biochemistry, Faculty of Biology and Biotechnology, Ruhr-University Bochum, Universitätsstraße 150, 44801 Bochum, Germany

4 Proteomics, Max Planck Institute of Biophysics, Frankfurt am Main, Germany

5 Structural Bioinformatic, Regensburg Center for Biochemistry, Regensburg Center for Ultrafast Nanoscopy, Faculty of Biology and Preclinical Medicine, University of Regensburg, Regensburg, Germany

6 Protein Crystallography, Faculty of Biology and Biotechnology, Ruhr-University Bochum, Bochum, Germany

7 Evolutionary Biochemistry Group, Max Planck Institute for Terrestrial Microbiology, Marburg, Germany

8 Proteomics, Max Planck Institute for Brain Research, Frankfurt am Main, Germany

9 Department of Biochemistry, Institute of Biosciences, University of Rostock, 18059 Rostock, Germany

10 Department Life, Light, Matter, University of Rostock, 18059 Rostock, Germany

Supplementary information

Supplementary discussion

PSII Preparation and biochemical characterization

A *Thermosynechococcus vestitus* BP-1 mutant line was created, in which the native Psb27-sequence was extended by an N-terminal Twin-Strep tag after the lipid-modified cysteine (supplementary Fig. S1). Psb27-containing PSII complexes were purified by Strep-tag affinity chromatography (ST-AC) after thylakoid-extraction with 1.2% (w/v) n-dodecyl-ß-d-maltoside (DDM) and 0.5% (w/v) Na-cholate (supplementary Fig. S2A). Most of the PSII reflects monomeric PSII with slightly different sizes, which indicates a mixture of different Psb27-containing PSII (supplementary Fig. S2B). Additionally, low amounts of dimeric PSII and PSI trimers are present. The separation into the subunits by SDS-PAGE revealed stoichiometric amounts of all major subunits and TS-Psb27 (supplementary Fig. S2C). Moreover, the low-molecular-weight proteins (LMWPs) PsbE, PsbF, PsbH, PsbI, PsbK, PsbL, PsbM, PsbT, PsbX, PsbZ, Psb30 and traces of PsbY were detected by MALDI-ToF-MS (supplementary Tab. S1). Most noteworthy, the PsbJ subunit is present, which is absent in the recent cryo-EM structures of Psb27-containing PSII complexes[1,2]. Psb34 and Psb28 were also detected by MS, although Psb28 was not clearly visible SDS-PAGE due to the intensive band of the TS-Psb27 (Supplementary Tab. S1, supplementary Data 1). The unknown band at around 25 kDa was assigned to Psb32 (Tll0404, Q8DLS4) by single-band LC-MS/MS (Supplementary Data 2). Similar to observations by Liu et al.[3] which used a His-tagged Psb27, PsbO was co-purified in sub-stoichiometric amounts. Several other proteins were identified by MS, including CyanoP, CyanoQ, PsbV, PsbU, FtsH as well as subunits from the membrane complexes NDH-1 and PSI (Supplementary Data 1). The Psb27-containing PSII fraction shows only residual oxygen evolution (363 ± 29 µmol $O_2 \cdot (mg\ Chl \cdot h)^{-1}$) compared to active PSII (5,000-6,000 µmol $O_2 \cdot (mg\ Chl \cdot h)^{-1}$) from *T. vestitus* obtained by similar preparations[4–6].

745 # Supplementary tables and figures

746 **Table S1: Cryo-EM data collection, refinement, and validation statistics.**

	Psb32-PSII (EMDB-52706) (PDB 9I83)	Psb27-PSII (EMDB-52705) (PDB 9I82)
Data collection and processing		
Magnification	29,000X	29,000X
Voltage (kV)	300	300
Electron exposure (e–/Å^2)	55	55
Defocus range (μm)	-0.5 to -3.0	-0.5 to -3.0
Pixel size (Å)	0.84	0.84
Symmetry imposed	C1	C1
Initial particle images (no.)	5,055,941	5,055,941
Final particle images (no.)	199,653	325,601
Map resolution (Å)	2.9	2.8
FSC threshold	0.143	0.143
Map resolution range (Å)	2.5-5.0	2.5-4.0
Map sharpening *B* factor (Å^2)	-81.7658	-91.0728
Refinement		
Initial model (PDB-ID)	3KZI 2Y6X (Psb27) 8C7I this publication (Psb32)	3KZI 2Y6X (Psb27)
Model Composition		
Non-hydrogen atoms	23676	20977
Protein atoms	20093	17491
Ligand atoms	3583	3486
B factors (Å)2 (Min/Max/Mean)		
Protein	12.93 / 161.67 / 67.32	14.46 / 143.79 / 55.93
Ligand	6.06 / 161.73 / 50.58	8.73 / 131.05 / 48.75
R.m.s. deviation		
Bond length (Å)	0.004	0.004
Bond angles (°)	0.885	0.879
Validation		
MolProbity score	1.39	1.10
Clash score	1.75	1.25
Rotamer Outliers (%)	2.20	1.16
Ramachandran plot		
Favored (%)	96.75	96.71
Allowed (%)	3.17	3.20
Outliers (%)	0.08	0.09

747

748

749 **Table S2: Crystal structure statistics.** Values in parentheses are for the highest resolution shell.

	sgpsb32_6
Diffraction Source	SLS PXII
Wavelength (Å)	0.975107
Temperature (K)	100
Detector	PILATUS 6M
Crystal-to-detector distance (mm)	435
Rotation range per image (°)	0.25
Total rotation range (°)	325
Exposure time per image (s)	0.1
Space group	$P6_122$
a, b, c (Å)	145.65, 145.65, 91.81
α, β, γ (°)	90, 90, 120
Resolution range (Å)	45.68-2.12 (2.18-2.12)
Total No. of reflections	1158546 (88765)
No. of unique reflections	32795 (2370)
Completeness (%)	99.9 (100)
Multiplicity	35.3 (37.5)
⟨I/σ(I)⟩	24.87 (1.01)
Rmeas (%)	13.0 (675.2)
CC1/2	100 (56.3)
Overall B factor from Wilson plot ($Å^2$)	64.1
Refinement statistics	
Reflections used in refinement	32779
Reflections used for R-free	1639
R-work	0.2504
R-free	0.2787
CC(work)	0.944
CC(free)	0.948
Number of non-hydrogen atoms	3165
macromolecules	3109
ligands	39
solvent	33
Protein residues	398
RMS(bonds)	0.004
RMS(angles)	0.58
Ramachandran favored (%)	96.43
Ramachandran allowed (%)	2.81
Ramachandran outliers (%)	0.77
Rotamer outliers (%)	1.17
Clashscore	5.18
Average B-factor	86.89
macromolecules	87.21
ligands	70.95
solvent	68.27
Number of TLS groups	2

750

751 **Table S3 Coordinating interactions of Psb32 with the other PSII subunits.** Listed are all specific
752 contacts between Psb32 and the rest of the complex as well as the number of van der Waals contacts.
753 Coloring according to figure 1.

Subunit 1	Subunit 2	Residue 1	Residue 2	Contact Type
Psb32	Psb27	Arg82	Ser102	H-Bond
Psb32	Psb27	Arg82	Ser103	H-Bond
Psb32	Psb27	Arg82	Pro105	Speficifc Van der Waals
Psb32	Psb27	Asp84	Asn106	H-Bond
Psb32	Psb27	Asp84	Arg107	H-Bond
Psb32	Psb27	Tyr85	Tyr104	Speficifc Van der Waals
Psb32	Psb27	4x		Van der Waals
Psb32	PsbV	Val118	Arg131	H-Bond
Psb32	PsbV	Arg152	Asp137	H-Bond
Psb32	PsbV	Glu184	Lys50	H-Bond
Psb32	PsbV	Glu189	Glu28	H-Bond
Psb32	PsbV	3x		Van der Waals
Psb32	PsbE	Tyr191	Pro52	Speficifc Van der Waals
Psb32	PsbE	Tyr191	Asp53	H-Bond
Psb32	PsbE	Lys192	Arg51	H-Bond
Psb32	PsbE	Lys194	Asp45	H-Bond
Psb32	PsbE	Thr197	Thr40	H-Bond
Psb32	PsbE	Tyr224	Arg18	Speficifc Van der Waals
Psb32	PsbE	25x		Van der Waals
Psb32	PsbF	Thr190	Phe42	H-Bond
Psb32	PsbF	Thr190	Gln44	H-Bond
Psb32	PsbF	Thr190	Gln44	H-Bond
Psb32	PsbF	Tyr221	Phe16	Speficifc Van der Waals
Psb32	PsbF	3x		Van der Waals

754

Table S4 Coordinating interactions of the D2 C-terminal tail in Psb32-PSII and the mature PSII complex. Listed are all contacts between the last five C-terminal residues of D2 and their interacting subunits within the immature Psb32-PSII assembly intermediate (PDB-ID: 9I83) and mature PSII (PDB-ID: 4PJ0). Coloring according to figure 1.

Subunit 1	Subunit 2	Residue 1 (in-file Numbering)	Residue 2 (in-file Numbering)	Contact Type
Psb32-PSII				
D2	D1	Pro347	Met331	Van der Waals
D2	CP47	Pro347	Phe383	Specific Van der Waals
D2	D1	Arg348	Val330	Van der Waals
D2	D1	Gly349	Val330	H-Bond
D2	D1	Gly349	Arg334	Van der Waals
D2	CP47	Asn350	Arg384	H-Bond
D2	CP47	Ala351	Phe383	Van der Waals
D2	CP47	Ala351	Arg384	Van der Waals
D2	CP47	Ala351	Arg384	Van der Waals
D2	CP47	Leu352	Phe383	Specific Van der Waals
D2	CP47	Leu352	Arg383	Van der Waals
Mature PSII				
D2	CP47	Pro347	Phe383	Van der Waals
D2	PsbU	Arg348	Lys104	H-Bond
D2	D1	Gly349	Val330	H-Bond
D2	D1	Gly349	Arg334	Van der Waals
D2	CP47	Gly349	Arg384	H-Bond
D2	D1	Asn350	Arg334	H-Bond
D2	D1	Asn350	His337	H-Bond
D2	PsbO	Asn350	Asn155	H-Bond
D2	D1	Ala351	His337	Van der Waals
D2	D1	Ala351	Asn338	Van der Waals
D2	PsbU	Ala351	Gly101	H-Bond
D2	PsbU	Ala351	Tyr103	Van der Waals
D2	PsbU	Ala351	Tyr103	Van der Waals
D2	D1	Leu352	His332	Van der Waals
D2	D1	Leu352	His337	Specific Van der Waals
D2	D1	Leu352	His337	Van der Waals

759
760 **Table S5: Proteins identified by MALDI-ToF and LC-MS/MS**

Accession	Gene name	Describtion	Detected by LC-MS	Detected by MALDI
P0A444	PsbA1	Photosystem II protein D1 1	+	
P0A446	PsbA2	Photosystem II protein D1 2	+	
Q8DIQ1	PsbB	Photosystem II CP47 reaction center protein	+	
Q8DIF8	PsbC	Photosystem II CP43 reaction center protein	+	
Q8CM25	PsbD1	Photosystem II D2 protein	+	
Q8DIP0	PsbE	Cytochrome b_{559} subunit alpha	+	+
Q8DIN9	PsbF	Cytochrome b_{559} subunit beta	+	+
Q8DJ43	PsbH	Photosystem II reaction center protein H	+	+
Q8DJZ6	PsbI	Photosystem II reaction center protein I	+	+
P59087	PsbJ	Photosystem II reaction center protein J	+	+
Q9F1K9	PsbK	Photosystem II reaction center protein K	+	+
Q8DIN8	PsbL	Photosystem II reaction center protein L	+	+
Q8DHA7	PsbM	Photosystem II reaction center protein M	+	+
P0A431	PsbO	Photosystem II manganese-stabilizing polypeptide	+	
Q8DH84	PsbP	PsbP protein	+	
Q8DIQ0	PsbT	Photosystem II reaction center protein T	+	
P0A386	PsbV	Cytochrome c_{550}	+	+
Q9F1R6	PsbX	Photosystem II reaction center X protein	+	
Q8DKM3	PsbY	Photosystem II protein Y	+	+
Q8DHJ2	PsbZ	Photosystem II reaction center protein Z	+	+
PSII associated				
Q8DG60	TS-Psb27	Photosystem II lipoprotein Psb27	+	
Q8DLJ8	Psb28	Photosystem II reaction center Psb28 protein	+	
Q8DLS4	tll0404	Tll0404 protein (Psb32)	+	
Q8DMP8	tsl0063	Tsl0063 protein (Psb34)	+	+
Q8DJE2	PsbV2	Cytochrome c_{550}-like protein	+	
Q8DJI1	Psb30	Photosystem II reaction center protein Ycf12/Psb30		+

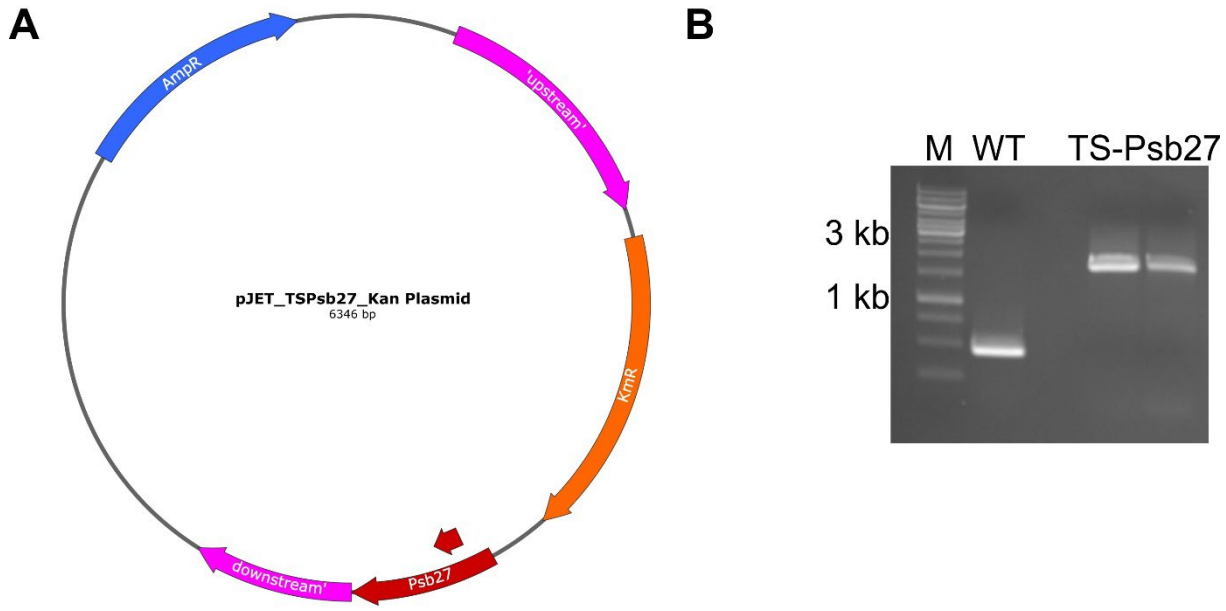

Figure S1: Construction of TwinStrep-tagged Psb27. **A)** Plasmid map used for the transformation. The plasmid contains resistance cassettes against ampicillin (blue) and kanamycin (orange). The up- and downstream regions are shown in pink and the Psb27 sequence and the TS-Tag (small arrow) are shown in red. **B)** Agarose gel electrophoresis of the PCR-Products of *T. vestitus* BP-1 (WT) and two TS-Psb27 mutants (see methods for primer details). A size standard (M), Thermo Scientific GeneRuler 1 kb DNA Ladder was applied.

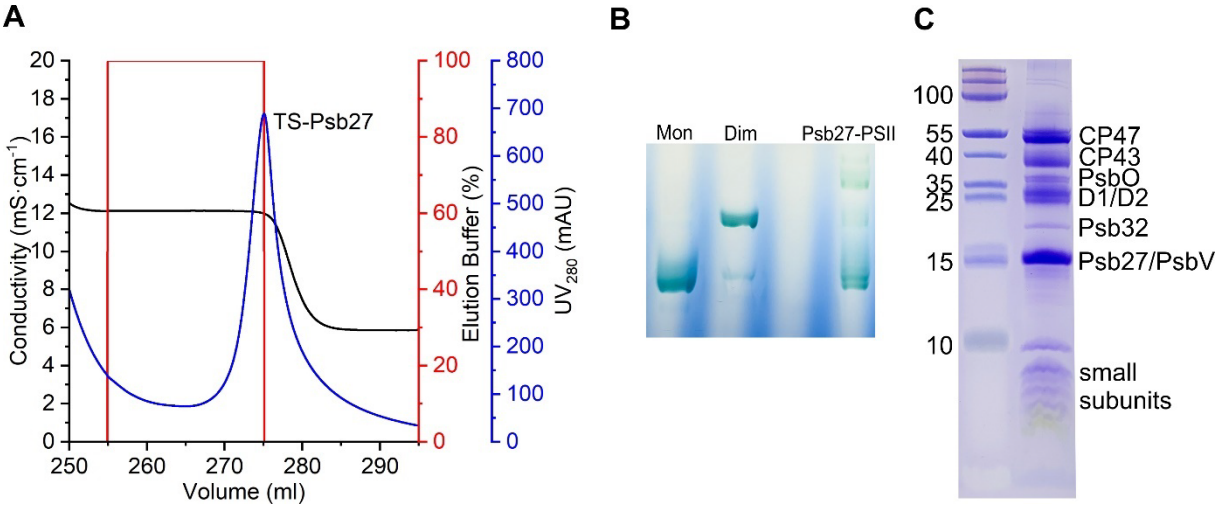

Figure S2: Preparation of PSII with TS-Psb27. A) Strep-Tag affinity chromatography (ST-AC) elution peak. The UV-absorption is shown in blue, the gradient of the elution buffer in red, and the conductivity in blue. The graphs shown are representative of several individual preparations. **B)** BN-PAGE and **C)** SDS-PAGE of purified PSII. A size standards (M), Thermofisher PageRuler #26616 was used for SDS-PAGE and PSII monomer/dimer purified by TS-tagged CP43 for BN-PAGE[5].

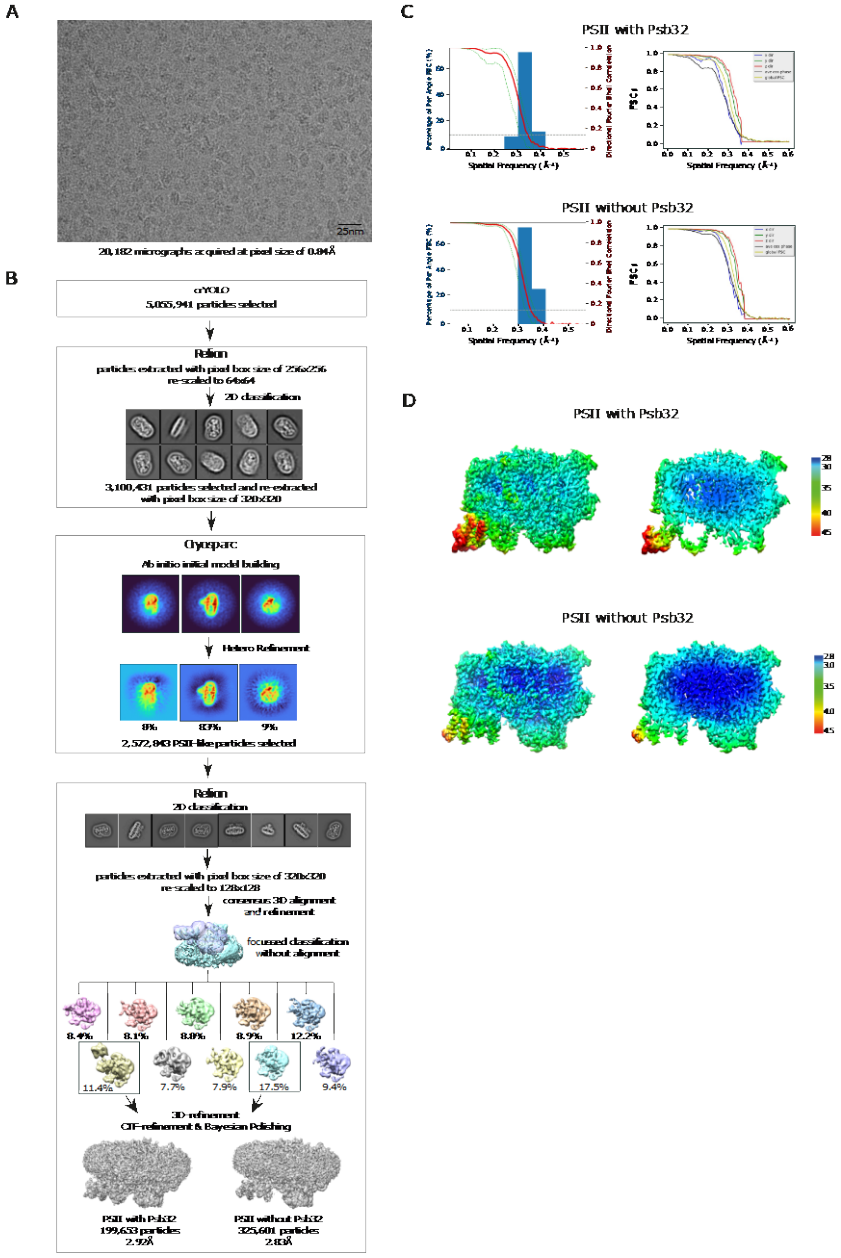

Figure S3: Cryo-EM data collection and processing scheme. **A)** Exemplary micrograph acquired on K3 (Gatan, 5760x4092 pixel) showing particle distribution on Quantifoil 2/1 grid-holes. **B)** Schematic of the image processing workflow. Particles were picked with crYOLO and extracted with RELION. After initial 2D classification, selected particles were used for ab initio model building and 3D-classification in Cryosparc. Particles belonging to the class resembling an intact PSII-particle were further classified in RELION (2D as well as focused classification using a mask). Classes resulting from focused refinement were refined and analyzed individually (not shown). Representatives of each identified unique conformer (with and without additional density in the mask region) were refined and particles belonging to the resulting two densities were subjected to CTF-refinement and Bayesian polishing before the final refinement. **C)** Plots showing the global (left plot) and directional (right plot) resolution for the two densities obtained in B), calculated using the "Remote 3DFSC Processing Server" web interface. For PSII with Psb32 and PSII without Psb32 a sphericity score of 0.947 and 0.970 and a global resolution (FSC-threshold = 0.143) of 2.99A and 2.86A were calculated, respectively. **D)** Local resolution as calculated by RELION mapped on the refined densities (left: surface view, right: cut-open view of central section).

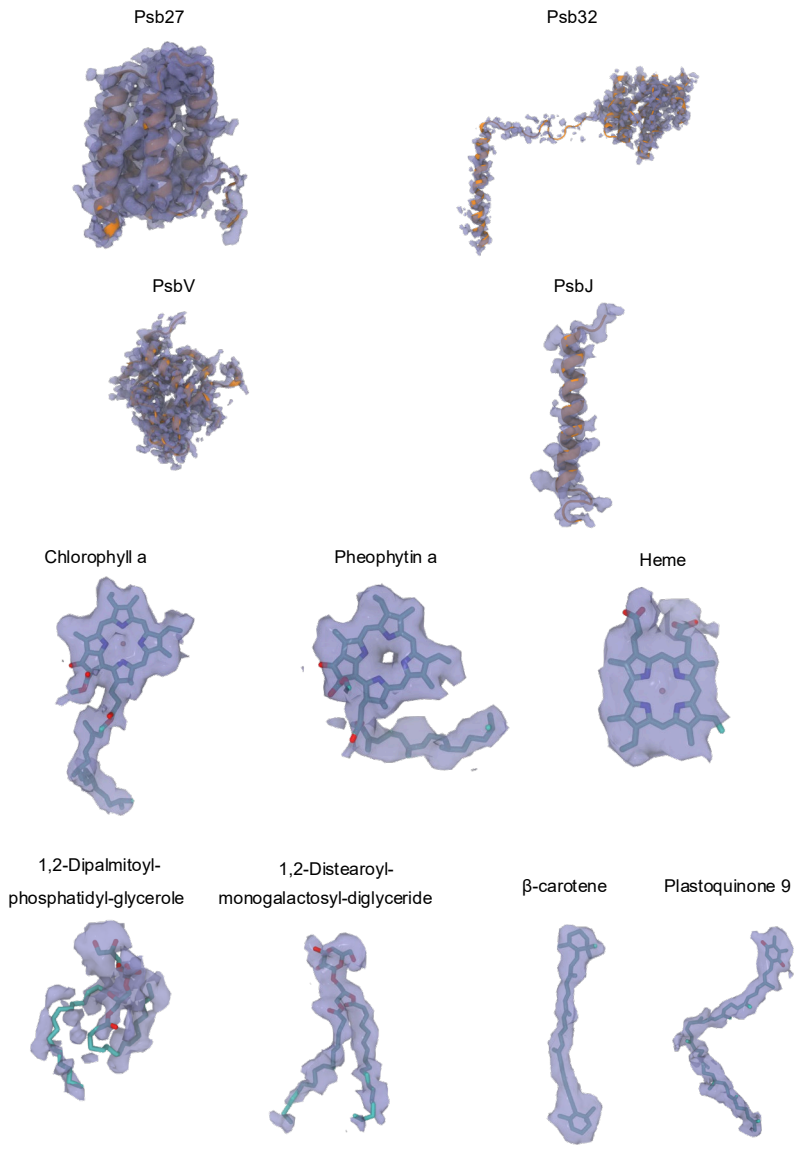

Figure S4: Comparison of structural model and density for Psb32-PSII. Fit of the structural model into the density map (transparent blue) for selected key subunits and cofactors of Psb32-PSII. The resolution is sufficient for accurate modeling of subunits and cofactors.

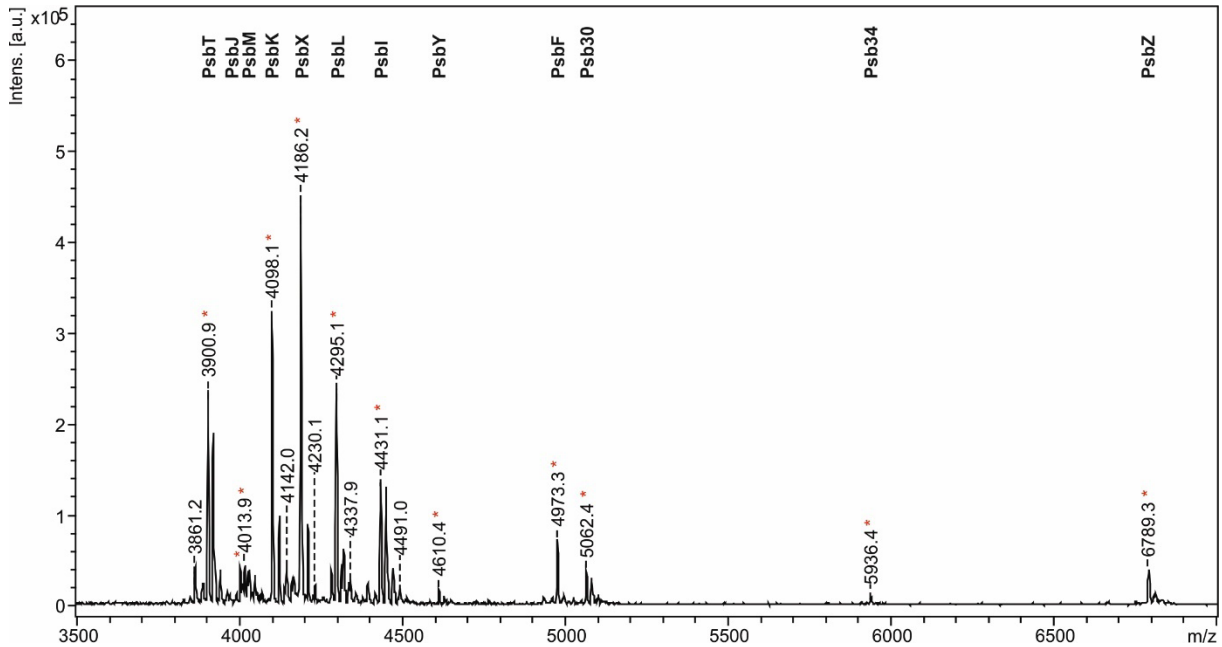

Figure S5: MALDI-ToF-MS spectra of the small proteins of PSII at the m/z range from 3,500 to 7,000. Annotation of the peaks was done according to[6–8]. Stars indicate modified peptides.

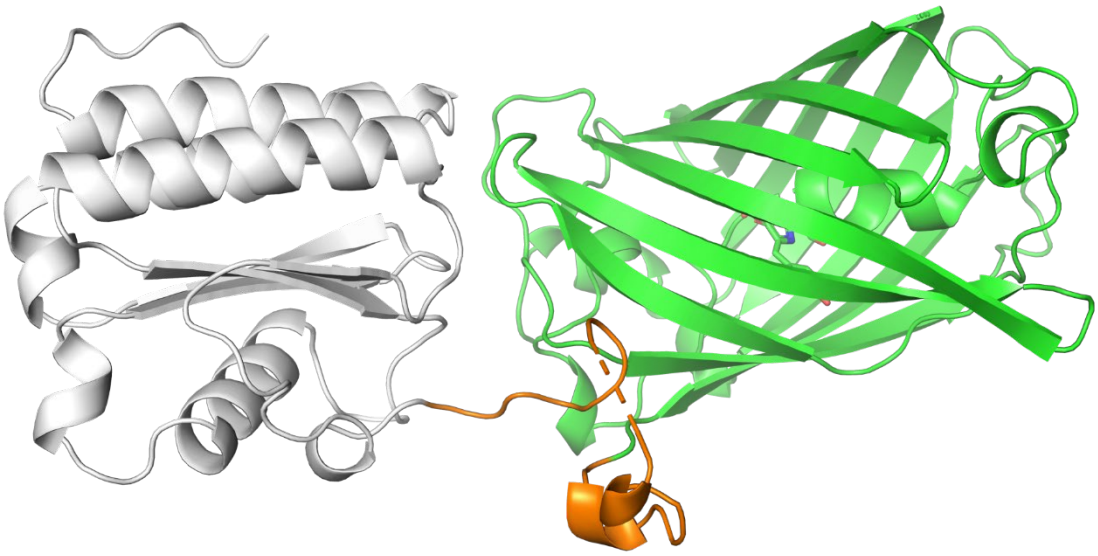

Figure S6: Psb32 crystal structure. Cartoon representation of the structure of the sfGFP-Psb32 fusion protein. The sfGFP is colored in green, Psb32 (residues 0 to 150 in PDB-ID 8C7I and residues 30-180 from Uniprot ID Q8DLS4) colored in grey. The partially disordered linker region is shown in orange.

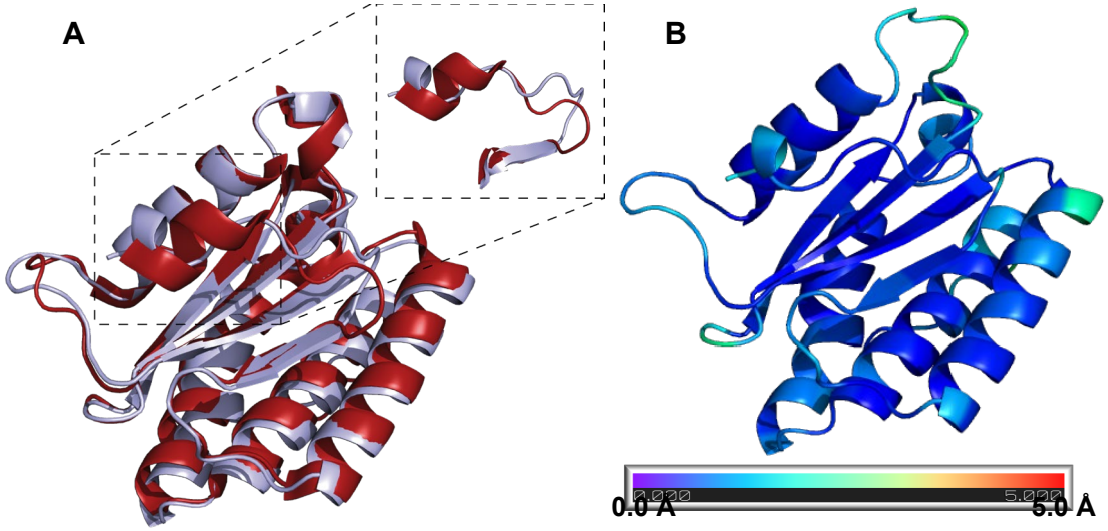

Figure S7: Comparison of Psb32 X-ray crystal structures. A) Cartoon representation of the here resolved X-ray crystal structure of Psb32 from *Thermosynechococcus vestitus* (light-blue, PDB-ID 8C7I) aligned to its *Arabidopsis thaliana* ortholog (red, PDB-ID 3PVH[9]). The structures are nearly identical, except for the extended C-terminus, which differs significantly in amino acid sequence. **B)** Depiction of the X-ray crystal structure of Psb32 colored according to the Cα root mean square deviation (RMSD) compared to the resolved globular domain within the cryo-EM model. The coloring ranges from 0 Å RMSD (deep blue) to 5 Å RMSD between these models.

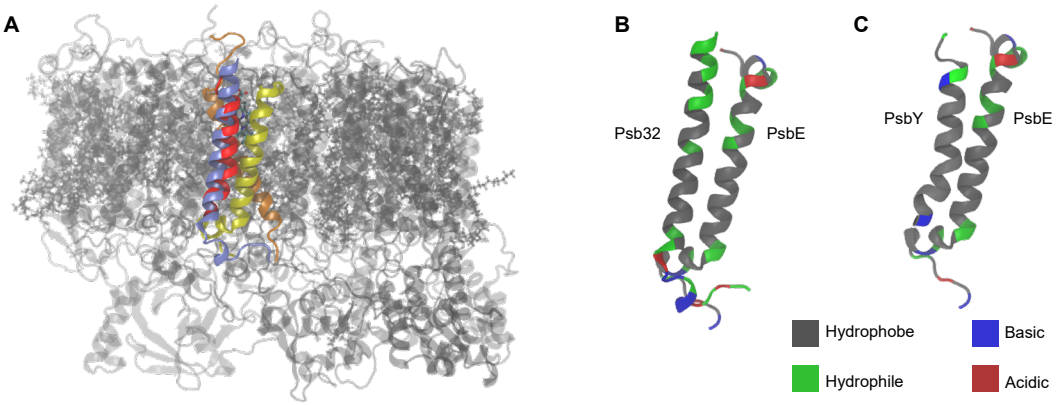

Figure S8: Assembly of Psb32 C-terminal Helix. A) Superposition of the mature PSII (PDB:4PJ0)[10] with Psb32-PSII shows that the C-terminal helix of Psb32 (light blue) occupies a similar position as PsbY (red), both shielding the heme of Cyt b_{559}. **B, C)** The different residue types of amino acids at the contact interface of are highlighted. **C)** Amino acid residue types at the contact interfaces of Psb32/PsbE and PsbY/PsbE, respectively. The abundance of hydrophobic residues and lack of compatible ionic or hydrophilic residues implies a mostly hydrophobic interaction for both Psb32 and PsbY.

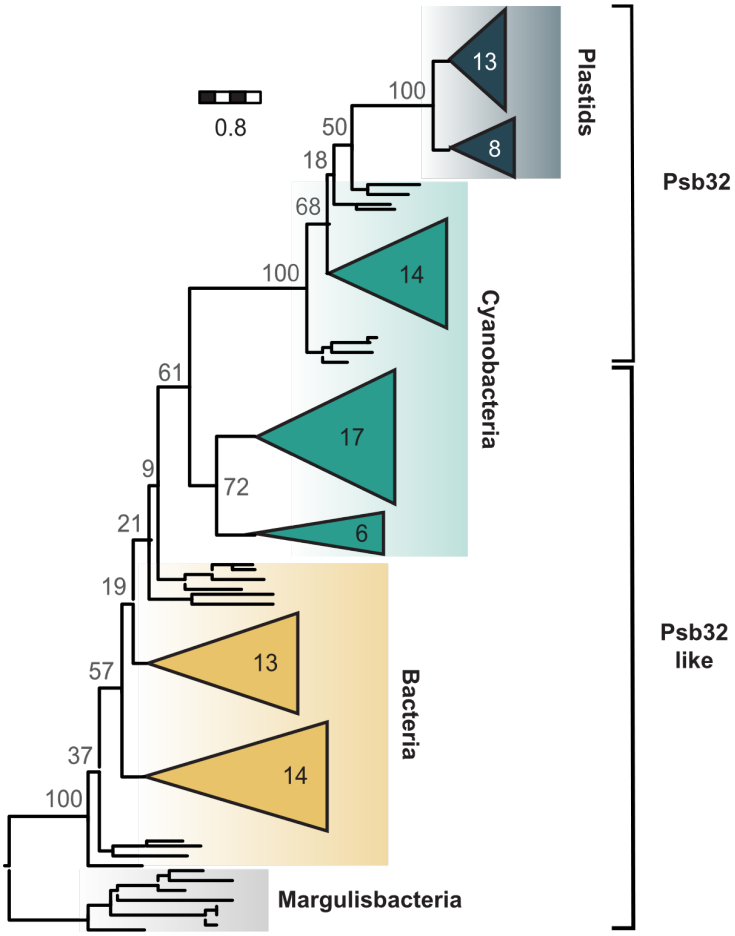

Figure S9: Phylogeny of Psb32 and Psb32-like homologues. Grey numbers next to nodes give non-parametric (Felsenstein) bootstraps, numbers in clades denote number of taxa per clade. The scale bar indicates how many amino acid substitutions happen on average per site along the horizontal branches.

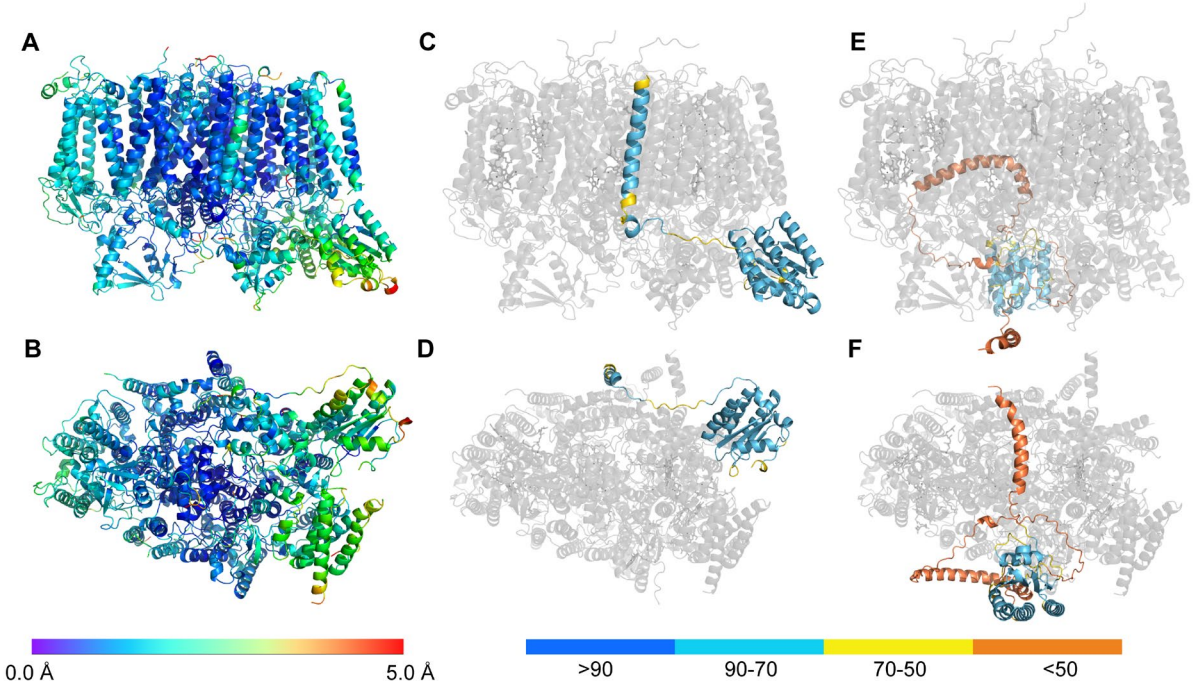

Figure S10: Structure predictions of Psb32 and the Psb32-like protein. Front (**A**) and bottom (**B**) view of the predicted Psb32-PSII colored according to the root mean square deviation of the Cα atom position compared to the cryo-EM model. Front (**C**) and bottom (**D**) view of the AlphaFold3[11] predicted Psb32-PSII complex. Psb32 is colored according to the AlphaFold pIDDT score. The front (**E**) and bottom (**F**) view of the predicted complex with the Psb32-like protein (colored by plDDT) reveals a shifted binding position and a low pIDDT score for all but the central globular domain. Interestingly, AlphaFold predicts the TMH of Psb32 in all suggested models with high confidence at the same position as indicated by the cryo-EM density. Also, the Psb32 globular domain is predicted at the same position as indicated by the cryo-EM density mainly coordinated by PsbV and Psb27. Though the cryo-EM model was neither involved in training nor as template for the prediction the whole predicted Psb32-PSII complex and the cryo-EM model agree very well with a low overall Cα–RMSD of 1.30 Å (2563 atoms). This low RMSD implies that AlphaFold can accurately predict the Psb32-PSII assembly intermediate, since the cryo-EM structure was not included in the training set or used as template. However, the predicted TMH of the Psb32-like protein shows low confidence and lacks coordinating interactions. The globular domain of the Psb32-like protein is positioned in close proximity to PsbA and CP43, far from the location of Psb32. The prediction results of the Psb32-PSII and a tentative Psb32-like protein PSII assembly intermediate indicate that the Psb32-like protein cannot form a PSII assembly intermediate and therefore does not function as an assembly factor.

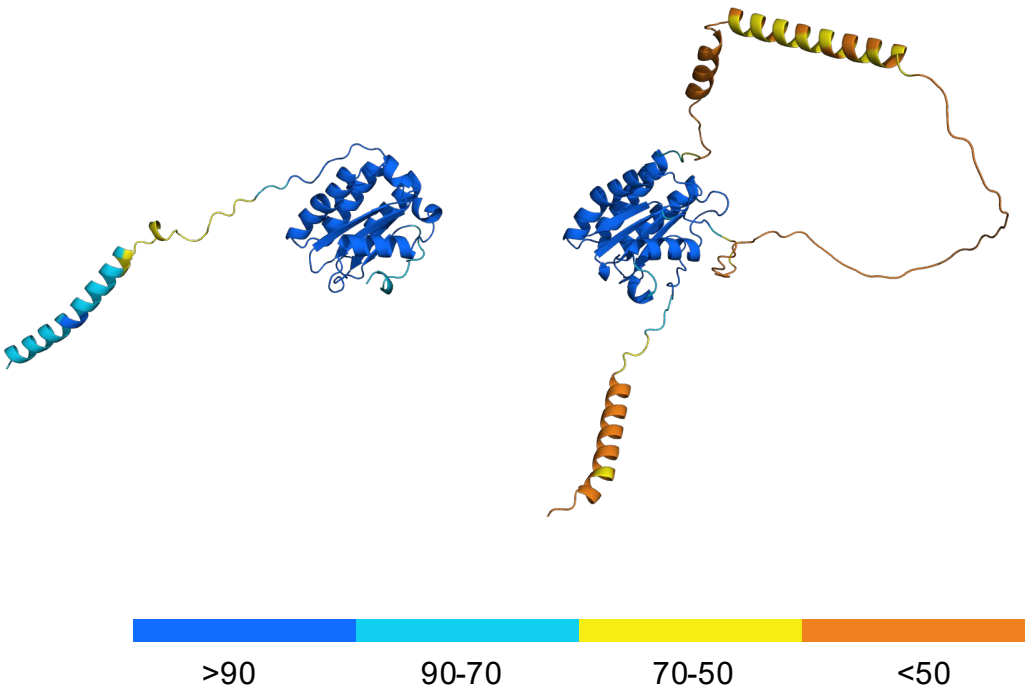

Figure S11. Comparison of predicted isolated Psb32 and Psb32-like protein structural models. The predicted Psb32 structure (**left,** colored according to their plDDT) shows high confidence in the globular domain of the protein and confidence in the C-terminal helix. The connecting unstructured linker shows partial low confidence. While the predicted Psb32-like protein structure (**right**) shows high confidence in the globular domain, its N- and C-terminal regions show low to very low confidence.

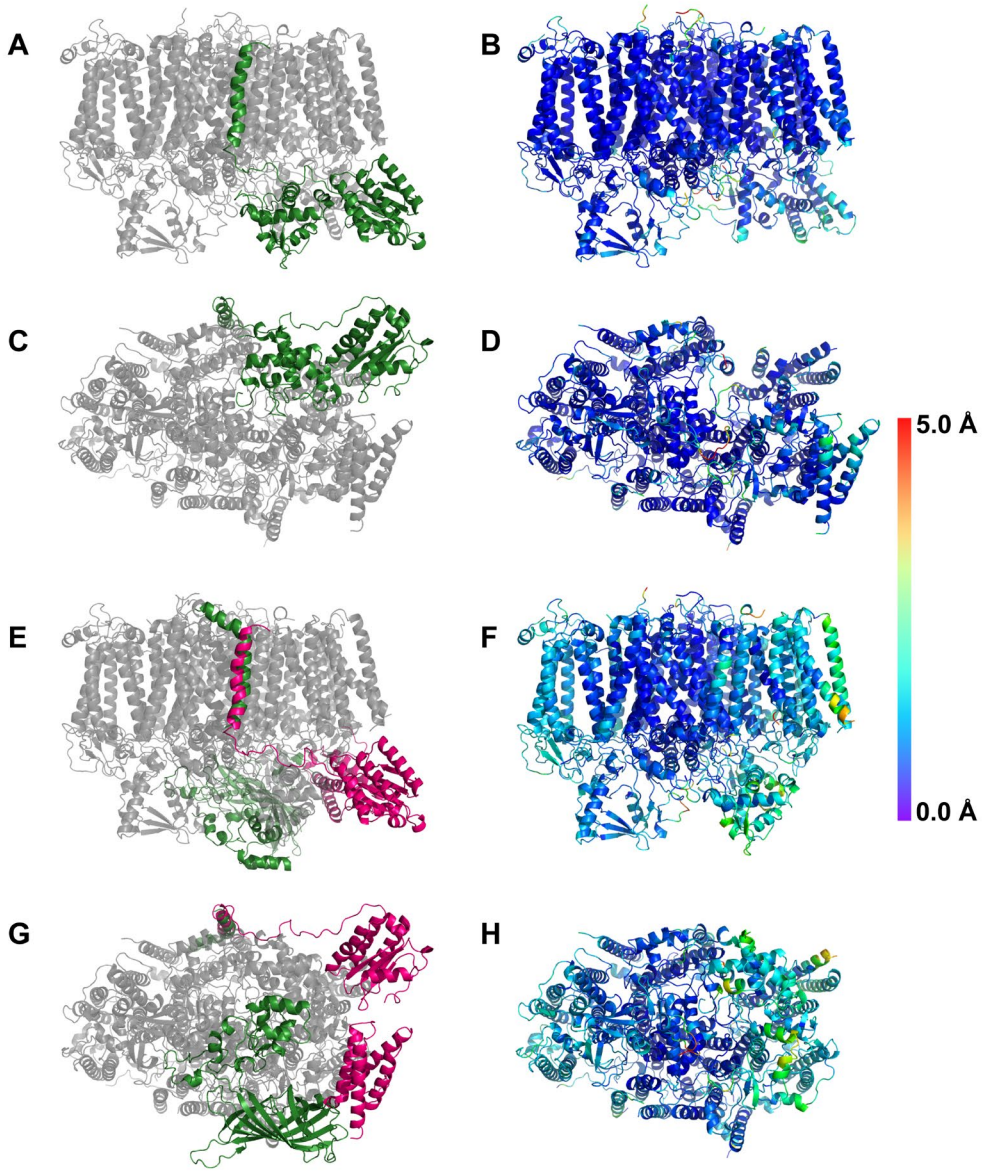

Figure S12: Changes within the PSII complex across the assembly. Front and bottom view of the leaving (red) and newly introduced (green) subunits upon switching from Psb27-PSII to Psb32-PSII (**A, C**) and switching from Psb32-PSII to the mature complex (**E, G**). Per-residue-colouring of the Cα-RMSD upon switching between Psb27-PSII and Psb32-PSII (**B, D**), and Psb32-PSII and the mature complex (**F, H**), respectively. The colouring ranges from 0 Å RMSD (deep blue) to 5 Å RMSD (red) between the respective models.

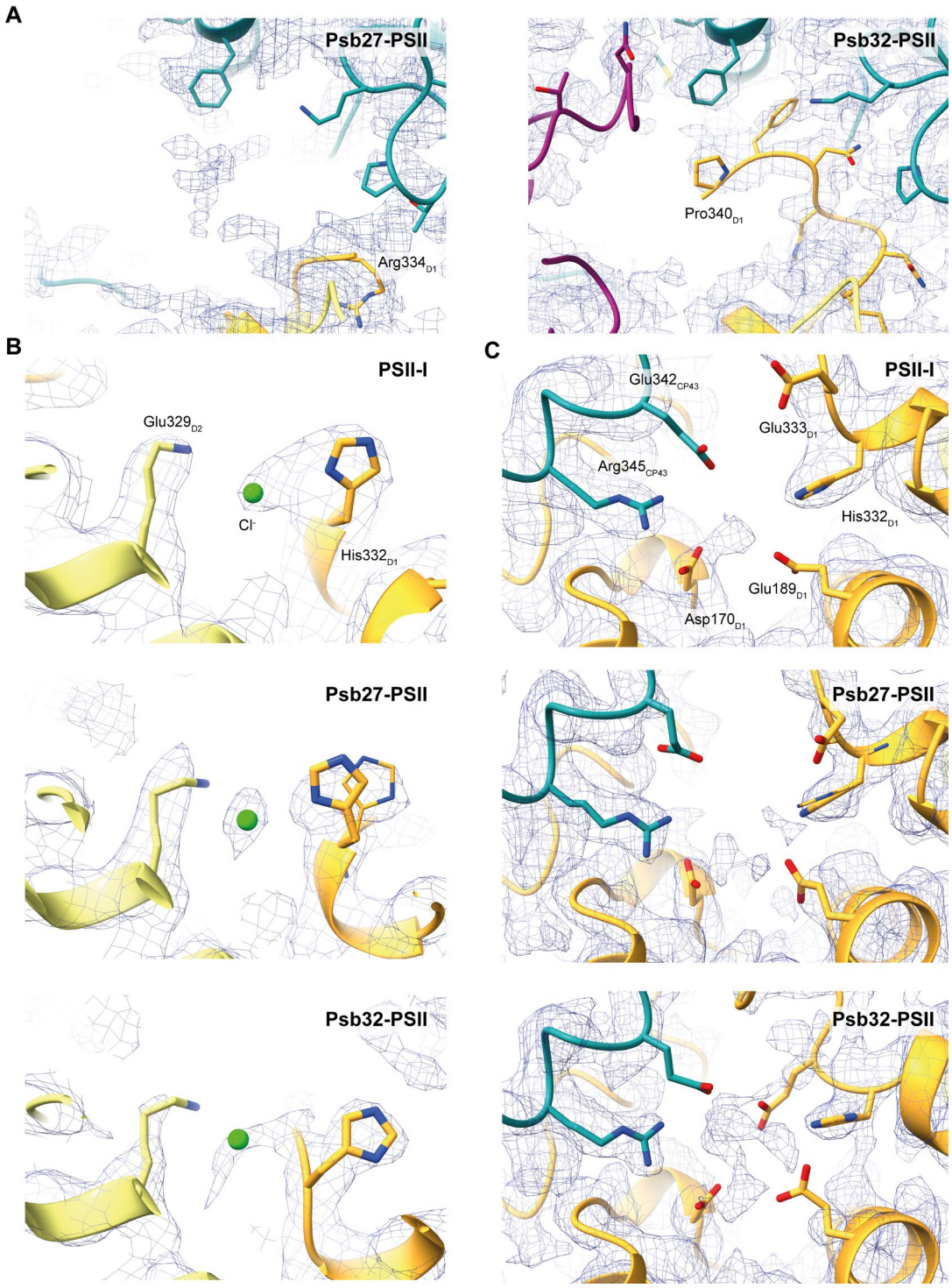

Figure S13: Cryo-EM density and model fitting around the OEC. A) Density fitting of Psb27-PSII D1 C-terminal loop (left) and Psb32-PSII D1 C-terminal loop (right). Maps are displayed at 2 σ. In Psb27-PSII, no defined density could be resolved beyond D1 Arg334 while in Psb32-PSII, no defined density could be resolved beyond D1 Pro340. **B)** Density fitting of His332 and chloride ion in PSII-I, Psb27-PSII and Psb32-PSII. **C)** Residues resolved around the OEC of PSII-I, Psb27-PSII and Psb32-PSII. For **B** and **C**, density maps of PSII-I, Psb27-PSII and Psb32-PSII are shown at 2.5 σ, 3.0 σ, and 3.5 σ, respectively.

References

1. Huang, G. *et al.* Structural insights into a dimeric Psb27-photosystem II complex from a cyanobacterium *Thermosynechococcus vulcanus*. *PNAS* **118,** e2018053118; 10.1073/pnas.2018053118 (2021).
2. Zabret, J. *et al.* Structural insights into photosystem II assembly. *Nat. Plants* **7,** 524–538; 10.1038/s41477-021-00895-0 (2021).
3. Liu, H., Roose, J. L., Cameron, J. C. & Pakrasi, H. B. A genetically tagged Psb27 protein allows purification of two consecutive photosystem II (PSII) assembly intermediates in *Synechocystis* 6803, a cyanobacterium. *The Journal of Biological Chemistry* **286,** 24865–24871; 10.1074/jbc.M111.246231 (2011).
4. Kuhl, H. *et al.* Towards structural determination of the water-splitting enzyme. Purification, crystallization, and preliminary crystallographic studies of photosystem II from a thermophilic cyanobacterium. *The Journal of Biological Chemistry* **275,** 20652–20659; 10.1074/jbc.M001321200 (2000).
5. Lambertz, J., Liauw, P., Whitelegge, J. P. & Nowaczyk, M. M. Mass spectrometry analysis of the photosystem II assembly factor Psb27 revealed variations in its lipid modification. *Photosynth Res,* Available online under https://doi.org/10.1007/s11120-021-00891-7; 10.1007/s11120-021-00891-7 (2021).
6. Lambertz, J. *et al.* Isolation of a novel heterodimeric PSII complex via strep-tagged PsbO **bioRxiv,** https://www.biorxiv.org/content/10.1101/2022.06.15.496312v1.full; 10.1101/2022.06.15.496312 (2022).
7. Nowaczyk, M. M. *et al.* Deletion of PsbJ leads to accumulation of Psb27-Psb28 photosystem II complexes in *Thermosynechococcus elongatus*. *Biochimica et Biophysica Acta (BBA)* **1817,** 1339–1345; 10.1016/j.bbabio.2012.02.017 (2012).
8. Boussac, A., Sellés, J., Hamon, M. & Sugiura, M. Properties of Photosystem II lacking the PsbJ subunit. *Photosynth Res* **Available online under https://doi.org/10.1007/s11120-021-00880-w**; 10.1007/s11120-021-00880-w (2021).
9. Wu, H.-Y., Liu, M.-S., Lin, T.-P. & Cheng, Y.-S. Structural and functional assays of AtTLP18.3 identify its novel acid phosphatase activity in thylakoid lumen. *Plant Physiol* **157,** 1015–1025; 10.1104/pp.111.184739 (2011).
10. Hellmich, J. *et al.* Native-like photosystem II superstructure at 2.44 Å resolution through detergent extraction from the protein crystal. *Structure (London, England : 1993)* **22,** 1607–1615; 10.1016/j.str.2014.09.007 (2014).
11. Abramson, J. *et al.* Accurate structure prediction of biomolecular interactions with AlphaFold 3. *Nature* **630,** 493–500; 10.1038/s41586-024-07487-w (2024).